

Title	Periportal macrophages protect against commensal-driven liver inflammation
Author(s)	Miyamoto, Yu; Kikuta, Junichi; Matsui, Takahiro et al.
Citation	Nature. 2024, 629, p. 901-909
Version Type	AM
URL	https://hdl.handle.net/11094/95817
rights	
Note	

Osaka University Knowledge Archive : OUKA

<https://ir.library.osaka-u.ac.jp/>

Osaka University

Title

Periportal macrophages protect against commensal-driven liver inflammation

Authors

Yu Miyamoto^{1,2,3}, Junichi Kikuta^{1,2,3,4}, Takahiro Matsui^{1,5}, Tetsuo Hasegawa¹, Kentaro Fujii^{1,2,3},
Daisuke Okuzaki^{2,6}, Yu-chen Liu^{2,6}, Takuya Yoshioka⁷, Shigeto Seno⁸, Daisuke Motooka^{2,6},
Yutaka Uchida^{1,2,3,4}, Erika Yamashita^{1,2,3}, Shogo Kobayashi⁹, Hidetoshi Eguchi⁹, Eiichi Morii⁵,
Karl Tryggvason¹⁰, Takashi Shichita¹¹, Hisako Kayama^{2,12}, Koji Atarashi¹³, Jun Kunisawa⁷,
Kenya Honda¹³, Kiyoshi Takeda^{2,12}, and Masaru Ishii^{1,2,3,4*}

Affiliations

¹Department of Immunology and Cell Biology, Graduate School of Medicine and Frontier Biosciences, Osaka University, Osaka, Japan

²WPI-Immunology Frontier Research Center, Osaka University, Osaka, Japan

³Life-omics Research Division, Institute for Open and Transdisciplinary Research Initiative, Osaka University, Osaka, Japan

⁴Laboratory of Bioimaging and Drug Discovery, National Institutes of Biomedical Innovation, Health and Nutrition, Osaka, Japan

⁵Department of Pathology, Graduate School of Medicine, Osaka University, Osaka, Japan

⁶Genome Information Research Center, Research Institute for Microbial Diseases, Osaka University, Osaka, Japan

⁷Laboratory of Vaccine Materials, Center for Vaccine and Adjuvant Research, National Institutes of Biomedical Innovation, Health and Nutrition, Osaka, Japan

⁸Department of Bioinformatic Engineering, Graduate School of Information Science and Technology, Osaka University, Osaka, Japan

⁹Department of Gastroenterological Surgery, Graduate School of Medicine, Osaka University, Osaka, Japan

¹⁰Cardiovascular & Metabolic Disorders Program, Duke-NUS, Duke-NUS Medical School, Singapore, Singapore

¹¹Laboratory for Neuroinflammation and Repair, Medical Research Institute, Tokyo Medical and Dental University, Tokyo, Japan

¹²Department of Microbiology and Immunology, Graduate School of Medicine, Osaka University, Osaka, Japan

¹³Department of Microbiology and Immunology, School of Medicine, Keio University, Tokyo, Japan

***Corresponding Author:**

Masaru Ishii, Department of Immunology and Cell Biology, Graduate School of Medicine and

Frontier Biosciences, Osaka University, 2-2 Yamada-oka, Suita, Osaka 565-0871, Japan

Tel: +81-6-6879-3880, Fax: +81-6-6879-3889, E-mail: mishii@icb.med.osaka-u.ac.jp

Abstract

The liver is the main gateway from the gut, and the unidirectional sinusoidal flow from portal to central veins constitutes heterogenous zones, including the periportal vein (PV) and pericentral vein zones¹⁻⁵; however, functional differences in the immune system in each zone remain poorly understood. Here, intravital imaging revealed that inflammatory responses were suppressed in PV zones. The zone-specific single-cell transcriptomics detected an immunosuppressive macrophage subset enriched in PV zones that highly expresses IL-10 and Marco, a scavenger receptor sequestering pro-inflammatory PAMPs/DAMPs, and consequently suppressing immune responses. Induction of the Marco⁺ immunosuppressive macrophages depended on gut microbiota, and especially, a specific bacterial family, Odoribacteraceae, was identified to induce this macrophage subset via its postbiotic, isoallo-lithocholic acid. Intestinal barrier leakage results in inflammation in PV zones, which was markedly augmented by Marco-deficient conditions. Chronic liver inflammatory diseases such as primary sclerosing cholangitis (PSC) and non-alcoholic steatohepatitis (NASH) showed decreased Marco⁺ macrophages. Functional ablation of Marco⁺ macrophages led to PSC-like inflammatory phenotypes related to colitis and exacerbated steatosis in NASH in animal experimental models. Collectively, commensal bacteria induce Marco⁺ immunosuppressive macrophages, consequently limiting excessive inflammation at the gateway. Failure of this self-limiting

system promotes hepatic inflammatory disorders such as PSC and NASH.

1 **Main text**

2 The mammalian liver comprises repetitive hexagonal units called lobules in which blood flows
3 unidirectionally from portal veins and hepatic arteries towards draining central veins. This
4 polarised blood flow creates concentration gradients along the portal-central axis for blood
5 substances, such as nutrients and oxygen, as well as physiologically active substances^{1,2}. Based
6 on this polarised liver structure, several reports have demonstrated the polarised functions of
7 the periportal vein (PV) and pericentral vein (CV) zones. For example, hepatocytes in PV zones
8 contribute to gluconeogenesis and cholesterol biosynthesis, whereas those in CV zones are
9 involved in glutamine and bile acid production³⁻⁵. Liver sinusoidal endothelial cells (LSECs)
10 produce different chemokines depending on their zonal location, which may guide the
11 positioning of each immune cell type in the tissue^{6,7}. In addition, hepatic stellate cells (HSCs)
12 and LSECs in CV zones are prone to pathological changes upon exposure to carbon
13 tetrachloride, thereby exhibiting overproduction of pathogenic collagens compared to those in
14 PV zones^{7,8}. The hepatic immune system consists of an asymmetric distribution of resident
15 immune cells, especially Kupffer cells (resident macrophages), with a greater density around
16 the portal veins^{6,9}, effectively preventing gut bacteria from entering the systemic circulation⁶.
17 Nevertheless, the spatial heterogeneity in hepatic immune functions has not yet been explored.

18 In this study, we first performed spatial transcriptomic analysis of murine liver specimens,
19 focusing on the immune/inflammatory system. We could distinguish between PV and CV zones

20 based on the specific expression of *Cyp2f2* and *Cyp2e1*, well-defined zonation markers for
21 hepatocytes in PV and CV zones, respectively¹⁰ (**Fig. 1a**), enabling the extraction of
22 differentially expressed genes in each zone. We then performed the Gene Ontology analysis
23 and selected immunity-related terms for detailed analysis. Periportally enriched immune
24 pathways included many processes involved in the negative regulation of the immune system
25 (**Fig. 1b**). This result suggested that immune/inflammatory responses are more repressed in PV
26 than in CV zones. To directly visualise immune responses in PV and CV zones respectively,
27 we used high-resolution intravital two-photon microscopy to assess the in situ behaviours of
28 locally activated inflammatory cells highly expressing lysozyme M-GFP (LysM-GFP), mainly
29 including neutrophils in the liver, using a laser damage-induced sterile inflammation model.
30 These experiments revealed that neutrophils preferentially accumulated at damage sites in CV
31 zones compared with those in PV zones (**Fig. 1c (top), 1d (left), Supplementary Video 1**).
32 Even in the steady-state liver, neutrophils were inclined to reside in CV zones than in PV zones
33 (**Extended Data Fig. 1, Supplementary Video 2**). Subsequently, we focused on the possible
34 role of resident macrophages in the spatial heterogeneity of inflammatory responses in PV/CV
35 zones. We intravenously administered clodronate liposomes (CLL) which specifically depleted
36 the resident macrophages but not the other phagocytic myeloid cells (**Supplementary Fig. 1a,**
37 **b**). We confirmed that CLL treatment did not alter the expression of most chemokines involved
38 in neutrophil recruitment and did not increase the neutrophil infiltration (**Supplementary Fig.**

39 **1b, c**). Once resident macrophages were depleted by CLL (in the resident mac-depleted group),
40 neutrophils were shown to be accumulated equally at damage sites in both PV and CV zones
41 (**Fig. 1c (bottom), 1d (right), Supplementary Video 3**). We also examined the in situ
42 behaviours of CX₃CR1-positive circulating monocytes/macrophages upon the laser-induced
43 tissue damages¹¹. We found their skewed accumulation in CV zones, similar to the case with
44 neutrophils (**Extended Data Fig. 2a-c**), which was cancelled by depleting resident
45 macrophages with CLL treatment (**Extended Data Fig. 2d,e**). These results suggest that
46 periportal resident macrophages suppress inflammatory responses, with a greater inhibitory
47 activity in PV zones.

48 To identify the immunosuppressive macrophage subset residing in PV zones, we developed
49 a novel method for collecting liver-resident immune cells based on their locational information
50 (*i.e.*, in PV or CV zones) using transgenic mice globally expressing photoactivatable-GFP (PA-
51 GFP) (**Fig. 1e, Supplementary Fig. 2a**). After in vivo staining with a **phycoerythrin (PE)-**
52 **conjugated** anti-E-cadherin antibody to demarcate PV zones⁶, the livers were excised and
53 freshly sectioned, followed by photoactivation in either the PV or CV zones using violet laser
54 under microscopic guidance. Photoactivated (GFP⁺) CD45⁺ immune cells were collected for
55 single-cell RNA sequencing, which provided single-cell transcriptomic data for 1,282 cells
56 from PV zones and 1,179 cells from CV zones, including all immune cell types in the murine
57 liver^{9,12} (**Fig. 1f, Supplementary Fig. 2b, c**). Kupffer cells (liver resident macrophages) are

58 characterised by the expression of *Adgre1* and *Clec4f* (coding F4/80 and CLEC4F,
59 respectively)¹³ (**Supplementary Fig. 2c, d**). Among the different immune cell types in the liver,
60 Kupffer cells can be further divided into at least two subpopulations based on their expression
61 patterns, tentatively termed ‘MP1’ and ‘MP2’. *Marco*, a class A scavenger receptor, was found
62 to be exclusively expressed in the MP2 population (**Fig. 1g, Supplementary Fig. 3**).
63 Additionally, typical anti-inflammatory cytokines, such as *Il10*, *Il1rn*, and *Tgfb1* were shown
64 to be elevated in MP2, indicating the immunosuppressive property of MP2 (**Fig. 1h**). To
65 investigate the spatial distributions of MP1/MP2 in each zone, we calculated a localisation
66 score defined as the ratio of the number of PV zone-derived cells to that of CV zone-derived
67 cells of a given subset: > 1 and < 1 indicate bias towards PV and CV zones, respectively (**Fig.**
68 **1f**). MP2 cells were substantially biased towards PV zones, whereas MP1 cells were biased
69 towards CV zones. Immunofluorescence staining ensured that *Marco*⁺ F4/80⁺ cells (MP2) were
70 exclusively concentrated in E-cadherin⁺ PV zones; however, *Marco*⁻ F4/80⁺ cells (MP1) were
71 equally scattered across the tissue (**Fig. 1i**). Additionally, we could validate the polarised
72 distribution of neutrophils in CV zones observed using histological analyses (**Extended Data**
73 **Fig. 1**) and confirmed the previous results representing periportal distribution of natural killer
74 T cells (NKT), CX₃CR1-expressing macrophages and T cells^{6,14}. The spatial transcriptomic
75 analysis also verified periportally polarised expression of the anti-inflammatory molecules,
76 *Il10*, *Il1rn*, and *Tgfb1*, which should be expressed in MP2 (**Supplementary Fig. 2e**).

77 Reanalyses of public murine datasets from the liver cell atlas⁹ (large-scale single-cell and
78 spatial transcriptomic data) could detect the presence and skewed distribution of Marco⁺ IL10⁺
79 MP2 population (**Extended Data Fig. 3a-d**). Furthermore, based on the reanalyses of public
80 human single-cell transcriptomic database¹⁵, MARCO- and IL10-expressing macrophage
81 subset could also be detected in the human liver, which should correspond to human MP2
82 (**Extended Data Fig. 3e, f**). This human MP2-like population was shown to be significantly
83 reduced in pathological conditions such as liver cirrhosis¹⁵ (**Extended Data Fig. 3g**). The
84 presence of human MP2 would be further supported by a previous report describing periportal
85 MARCO⁺ ‘non-inflammatory’ macrophages in the human liver¹⁶. These reanalyses of public
86 databases demonstrate that Marco⁺ immunosuppressive macrophages are commonly present in
87 peri-portal vein regions in mice and humans.

88 Next, we examined the molecular mechanisms underlying the immunosuppressive action
89 of MP2 by focusing on interleukin-10 (IL-10) and Marco. Comparative quantification of *Il10*
90 expression in all the immune and non-immune cell types revealed that MP2 was the major IL-
91 10 producer in the liver (**Fig. 2a, b**). We validated the increased transcriptional activity of *Il10*
92 in MP2 compared to that in MP1 using *Il10*-Venus reporter mice (**Extended Data Fig. 4a**). To
93 examine whether IL-10 signalling affects immune responses in PV zones, we treated mice with
94 an anti-IL-10R blocking antibody and performed intravital imaging to observe neutrophil
95 behaviours upon the laser-induced tissue damages. Neutrophil accumulation at damage sites in

96 PV zones was significantly increased by IL-10 signalling **blockade** (**Fig. 2c, Supplementary**
97 **Video 4**), indicating that IL-10 from MP2 is crucial for limiting inflammatory responses in PV
98 zones. To investigate the molecular mechanism by which IL-10 regulates neutrophil behaviours,
99 we investigated its effects on the liver-resident cells, particularly in liver sinusoidal endothelial
100 cells (LSECs) and Kupffer cells. We first investigated the spatial expression of the adhesion
101 molecule ICAM-1, the ligand of α_M integrin (Mac1 or CD11b), which has reportedly been
102 crucial for neutrophil adhesion to the liver¹⁷. We classified LSECs based on CD117 expression:
103 CD117-positive and CD117-negative indicate peri-central venous and peri-portal LSECs,
104 respectively⁶, and revealed that ICAM-1 expression was significantly higher in CD117⁺
105 LSECs than that in CD117⁻ LSECs (**Extended Data Fig. 5a-c**). Next, we examined whether
106 administering anti-IL-10R antibodies could increase ICAM-1 expression on the periportal
107 CD117⁻ LSECs, and found that ICAM-1 expression increased in peri-portal LSECs (**Extended**
108 **Data Fig. 5d**). These results suggest that IL-10 locally produced by MP2 suppresses ICAM-1
109 expression on LSECs, thereby inhibiting neutrophil adhesion to the PV zones. Furthermore,
110 we found that blockade of IL-10 signalling elevated the expression level of chemokines, *Cxcl1*
111 and *Cxcl2* in Kupffer cells and periportal LSECs, respectively (**Extended Data Fig. 5e**). These
112 chemokines activate the “inside-out” signalling of integrins in neutrophils, which rapidly
113 changes the integrin structure from the bent form to the upright form, and enhances its binding
114 affinity to the ligands¹⁸. We also confirmed an increase in staining intensity of α_M integrin on

115 neutrophil using fluorescein isothiocyanate (FITC)-conjugated antibodies when blocking IL-
116 10 signalling (**Extended Data Fig. 5f, g**). Additionally, we observed that **blockade** of IL-10R
117 increased the number of resident Kupffer cells expressing TIM-4, which is known as a marker
118 for endogenous Kupffer cells differentiated from embryonic stem cell progenitors¹⁹, but their
119 polarised distribution was retained (**Supplementary Fig. 4**). The increased density of Kupffer
120 cells with elevated chemokine expressions may synergistically promote neutrophil adhesion to
121 LSECs. Therefore, IL-10 locally secreted from MP2 may act on LSECs and Kupffer cells in
122 periportal regions, suppressing neutrophil adhesion in the two distinct manners. However,
123 administering anti-IL-10R antibodies itself did not affect the number of infiltrating neutrophils
124 in the liver (**Extended Data Fig. 5h**).

125 Flow cytometrical analysis detected a positive correlation between Marco expression and
126 *Il10* transcriptional activity in Kupffer cells (**Extended Data Fig. 4b**), suggesting the
127 functional role of Marco for immunosuppressive (IL-10 producing) activity. Next, we
128 evaluated *Il10* mRNA expression in wild-type (*Marco*^{+/+}) and *Marco* knockout (*Marco*^{-/-})
129 Kupffer cells and found that *Il10* expression was significantly decreased under *Marco*-deficient
130 conditions (**Extended Data Fig. 4c**). **This result suggests** that signalling downstream of Marco
131 stimulates the production of anti-inflammatory cytokines, such as IL-10. Intravital imaging
132 using the laser-induced damage model also verified that *Marco* knockout animals exhibited
133 enhanced inflammatory responses to the damages in PV zones due to the lack of IL-10 signals

134 (Fig. 2d, Extended Data Fig. 4c, Supplementary Video 5), suggesting a critical function for
135 the Marco-IL-10 axis for exerting the anti-inflammatory effects of MP2.

136 Marco is known as a scavenger receptor for damage-associated molecular patterns
137 (DAMPs) and a broad range of polyanionic substances released from bacteria²⁰⁻²². Since the
138 expression level of Marco in MP2 is significantly higher than those of other pattern recognition
139 receptors, such as TLR2 and TLR4, in periportally residing cells (Supplementary Fig. 5), we
140 hypothesised that Marco may also directly contribute to the immunosuppressive phenotype in
141 PV zones by sequestering these immunostimulatory factors^{20,23,24}. To address this issue, we
142 visualised the pathogen-capturing activity of Marco⁺ and Marco⁻ Kupffer cells in vitro and in
143 vivo, and demonstrated that Marco⁺ Kupffer cells preferentially captured fluorescently labelled
144 bacteria (Extended Data Fig. 6), suggesting that Marco⁺ MP2 Kupffer cells exert an anti-
145 inflammatory effect via Marco-dependent sequestration of immunogenic pathogens, in
146 addition to producing abundant anti-inflammatory cytokines, such as IL-10.

147 The liver is directly connected to the gut via the portal vein. Gut commensal microbes or
148 their components, such as lipopolysaccharide (LPS) or metabolites, can easily flow into the
149 liver through the portal vein²⁵. Next, we examined the effect of gut commensals on the
150 generation and function of MP2 Kupffer cells. We quantified the MP2 subset in specific
151 pathogen-free (SPF), germ-free (GF), and antibiotic-treated (ABX) mice. To analyse the
152 contribution of pathogen-associated molecular patterns (PAMPs), we compared the findings

153 with those from MyD88 knockout mice (MyD88^{-/-}) lacking a critical downstream adaptor
154 protein of PAMP receptors. The absolute numbers of sinusoidal F4/80⁺ macrophages (Kupffer
155 cells) were almost the same under all conditions, irrespective of their location within a lobule.
156 However, the percentages of Marco⁺ MP2 in GF, ABX, and MyD88^{-/-} mice were significantly
157 decreased compared to those in SPF controls (**Fig. 3a, b, c**). With a decrease in MP2, both
158 Kupffer cells and tissue lysates exhibited reduced *Ill10* expression under gut commensal
159 bacteria-depleted conditions compared to SPF controls (**Fig. 3d, e**). To examine whether the
160 decrease in MP2 by depleting gut commensal microbes affects inflammatory responses in PV
161 zones, we performed intravital imaging using antibiotic-treated mice to detect local
162 inflammatory responses upon the laser-induced damages. Neutrophil accumulation in PV zones
163 was significantly enhanced by gut commensal depletion (**Fig. 3f, Supplementary Video 6**),
164 suggesting the critical role of commensal microbe-induced MP2 in the immunosuppressive
165 activity within PV zones.

166 Coincidentally, we found that MP2 numbers varied between mice under different housing
167 conditions (SPF-A and SPF-B mice). A larger population of MP2 was observed in SPF-A (**Fig.**
168 **4a**). We then performed 16S ribosomal RNA (rRNA)-sequencing analysis using the colorectal
169 contents and identified five bacterial candidates that might induce MP2 (**Extended Data Fig.**
170 **7a-c**). Based on the **positive** correlation between the relative abundance of bacteria and the
171 percentage of Marco⁺ MP2, we focused on a bacterial family, Odoribacteraceae, which belongs

172 to the order Bacteroidales and has recently been shown to be involved in the longevity of
173 “centenarians”²⁶ (Fig. 4b, c). To determine whether Odoribacteraceae contributes to MP2
174 induction, we inoculated an Odoribacteraceae strain (Odori) or a *Bacteroides stercoris* strain
175 (Stercoris) as the negative control into germ-free mice. In parallel, we transplanted Odori or
176 Stercoris into antibiotic-treated mice and kept the mice with SPF mice in the same cage.
177 Although neither Stercoris nor Odori alone significantly induced MP2 (Fig. 4d), MP2
178 induction was augmented under symbiosis of Odori and other commensals (Fig. 4e). These
179 results indicated that Odoribacteraceae is critical but not sufficient for inducing MP2.
180 Odoribacteraceae is reportedly associated with bile acid metabolism in the gut lumen and
181 contributes to the production of isoallo-lithocholic acid (isoallo-LCA) from chenodeoxycholic
182 acid-derived metabolites, such as 3-oxoallo-LCA and Δ^4 -isoLCA, which are supplied by other
183 commensals^{26,27}. We measured isoallo-LCA contents in the faeces under the conditions of GF,
184 gnotobiotte with Odori alone, and SPF with/without Odori and confirmed that concentration of
185 isoallo-LCA was more than 10-fold higher in the SPF condition with Odori compared with that
186 in other conditions (Fig. 4f). This suggests that the symbiosis of Odori and other bacteria is
187 necessary for a sufficient supply of isoallo-LCA. Finally, we examined whether oral
188 administration of isoallo-LCA enhanced MP2 induction and revealed that isoallo-LCA
189 significantly stimulates the induction of Marco⁺ Kupffer cells and increases the expression
190 levels of *Ill10* mRNA (Fig. 4g, h), suggesting that the effect of Odoribacteraceae on MP2

191 induction is partly mediated by the postbiotic activity such as producing isoallo-LCA.

192 Regarding the physiological significance of the preferential distribution of MP2 in PV
193 zones, a plausible hypothesis is that specific amounts of gut commensals or their related
194 DAMPs/PAMPs can constitutively reach the liver via the portal vein²⁵, and MP2 may protect
195 against unfavourable inflammatory responses to such pathogens, especially at the entrance of
196 the liver, that is, hepatic periportal regions. This immunomodulatory mechanism would become
197 critical when the intestinal barrier is impaired, causing an increased number of pathogens to be
198 translocated into the liver, as observed in patients with colitis²⁸, non-alcoholic fatty liver
199 disease^{29,30}, autoimmune hepatitis^{31,32}, obesity³³, and diabetes³³. To verify this hypothesis, we
200 generated a dextran sodium sulphate (DSS)-induced acute colitis model using *Marco*^{+/+} (wild-
201 type) and *Marco*^{-/-} (knockout) mice and analysed inflammatory responses in the liver. In this
202 model, 1% DSS was orally administered for 1 week, and the livers were analysed after an
203 additional 4 days of normal water feeding (**Extended Data Fig. 8a**). In the results, Kupffer
204 cells from *Marco*^{-/-} mice exhibited decreased production of anti-inflammatory cytokines
205 compared with those from wild-type controls (**Extended Data Fig. 8b**), and consistently,
206 intravital imaging revealed substantially higher infiltration of inflammatory neutrophils into
207 the liver in *Marco*^{-/-} mice on day 11 (**Extended Data Fig. 8c, d, Supplementary Video 7**). In
208 accordance with the occurrence of the inflammation, *Marco*^{-/-} mice exhibited a significant
209 reduction in body weight (**Extended Data Fig. 8e**). Next, we introduced a mouse model of

210 chronic colitis by repetitive challenges with DSS to analyse the effect of chronic gut
211 inflammation on the liver (**Fig. 5a**), representing a significant increase in inflammatory
212 lymphocytes (T helper 17 cell: Th17) and neutrophils in the liver of *Marco*^{-/-} mice compared
213 to those in wild-type controls (**Fig. 5b, c**). Intravital imaging indicated an accumulation of
214 inflammatory neutrophils near the portal veins in *Marco*^{-/-} mice (**Fig. 5d, Supplementary**
215 **Video 8**). Consistently, serum markers for hepatic damage, including alanine aminotransferase
216 (ALT) and aspartate aminotransferase (AST), were elevated in *Marco*^{-/-} mice (**Fig. 5e**).
217 Furthermore, the expression levels of the fibrosis markers, *Timp1* and *Colla1*³², were also
218 increased, leading to type I collagen accumulation in periportal areas in *Marco*^{-/-} mice (**Fig. 5f,**
219 **g**). Such phenotypes in the *Marco*-deficient condition resemble those observed in chronic
220 human inflammatory liver diseases, such as primary sclerosing cholangitis (PSC). Primary
221 sclerosing cholangitis, an intractable disease of unknown origin that is characterised by chronic
222 inflammation around the bile duct and portal vein regions, leads to progressive fibrosis and
223 sclerosis in these areas^{34,35}. Notably, PSC is often complicated by inflammatory bowel diseases
224 and has been associated with microbial translocation from the inflamed gut^{34,36,37}. Using
225 clinical liver samples of patients with PSC as well as control liver specimens (six PSC and nine
226 normal control samples), we performed immunofluorescence staining to detect *Marco*⁺ and
227 *Marco*⁻ macrophages, demonstrating that the number of periportal *Marco*⁺ macrophages,
228 corresponding to MP2 in the murine liver, was significantly decreased in the PSC livers

229 compared to those in the controls. However, the number of total macrophages was comparable
230 between PSC and control liver specimens (**Fig. 5h, i**). These results may suggest that Marco-
231 expressing macrophages are present in the human liver, which could be associated with chronic
232 inflammatory liver diseases, such as PSC.

233 Next, we examined the possible roles of MP2 Kupffer cells in non-alcoholic fatty liver
234 disease (NAFLD)/non-alcoholic steatohepatitis (NASH), a common and intractable chronic
235 inflammatory disorder in the liver, often complicated with the leaky gut syndrome^{29,30}. Based
236 on the reanalysis of the single-cell data from patients with cirrhosis, the MP2 population was
237 reduced in patients with NAFLD compared with the normal controls (**Extended Data Fig. 3g**),
238 implying that MP2 might be involved in the disease progress. To reveal the relationship
239 between MP2 abundance and NAFLD/NASH development, we used a murine NASH/NAFLD
240 model by feeding a methionine-/choline-deficient high-fat (MCDHF) diet to mice for up to 6
241 weeks and harvested the livers in 2-week increments (**Extended Data Fig. 9a**). As a result, the
242 resident Marco⁺ TIM-4⁺ MP2 population was significantly declined by 64.5 % in the first 2
243 weeks (**Extended Data Fig. 9b, c**), which was inversely correlated to the occurrence of
244 inflammatory symptoms, such as elevation of serum AST/ALT and neutrophil infiltration
245 (**Extended Data Fig. 9d-i**). The correlation coefficients between MP2 presence and these
246 symptoms were $R = -0.82$ for AST, $R = -0.76$ for ALT, and $R = -0.59$ for neutrophil
247 accumulation, indicating strong negative correlations (**Extended Data Fig. 9e, g, i**). These

248 results suggest that the severity of the disease activity depends on the paucity level of MP2. We
249 then fed MCDHF diet to *Marco*^{-/-} (knockout) mice lacking the anti-inflammatory functions of
250 MP2 and detected a more severe liver inflammation (**Extended Data Fig. 9j**) and deteriorated
251 liver histopathology representing a more severe steatosis around the portal veins (**Extended**
252 **Data Fig. 9k. l**). The low value of AST/ALT ratio in *Marco*^{-/-} mice implies the stress-induced
253 damages in PV zones or more advanced fatty liver disease in *Marco*^{-/-} mice (**Extended Data**
254 **Fig. 9m**). We also verified that *Marco*⁺ MP2 was significantly decreased in human
255 NAFLD/NASH patients (seven samples) compared to the normal controls (nine samples)
256 (**Extended Data Fig. 9n-p**). The pathohistological samples can be classified based on the
257 severity of NAFLD/NASH groups according to the ‘Matteoni scoring system’³⁸, and we could
258 demonstrate that the number of MP2 was remarkably decreased in NASH (more severe) group,
259 compared to those in NAFLD (less severe) group (**Extended Data Fig. 9p**). These results may
260 suggest that Marco-expressing macrophages could be associated with the progression of
261 chronic inflammatory liver diseases, such as NAFLD/NASH as well as PSC.

262 The spatial heterogeneity of constituent cells is critical for tissue integrity. By combining
263 in vivo spatiotemporal imaging and single-cell transcriptomic analyses, we demonstrated the
264 heterogenous immune responsiveness in specific liver segments and newly identified an
265 immunosuppressive Marco-expressing resident macrophage (Kupffer cell) subset, designated
266 as MP2, which preferentially localises in PV zones. The presence of PV-polarised *Marco*⁺

267 immunosuppressive Kupffer cells are further supported by previous studies showing higher
268 phagocytic function of periportal Kupffer cells³⁹ and IL-10 production in response to PAMPs
269 stimulation⁴⁰. Scavenging exogenous toxins, including bacteria, PAMPs, and DAMPs, have
270 been demonstrated to serve as a firewall in the body^{41,42}; the concept is well consistent with the
271 function of Marco demonstrated in this study. In 2021, Bleriot *et al.* and Simone *et al.* proposed
272 subsets of Kupffer cell, KC1 and KC2^{43,44}. KC2 was regarded as a minor population expressing
273 CD206 and ESAM as markers for this specific population and involved in regulating oxidative
274 stress under fatty liver conditions⁴³ and activation of CD8⁺ cytotoxic T cells during hepatitis B
275 virus infection⁴⁴. Nevertheless, regarding the KC2, an immunosuppressive phenotype or
276 polarised distribution towards PV zones has not been reported, and we concluded that
277 KC1/KC2 is a conceptually different classification from MP1/MP2 in this study. Nevertheless,
278 based on the cell markers, we also checked that the Marco⁺ MP2 subset does not belong to
279 KC2 but instead belongs to KC1 (**Extended Data Fig. 10a-c**). Therefore, MP2 can be redefined
280 as a subset of KC1 and be referred to as “Marco⁺ KC1” (**Extended Data Fig. 10d**).

281 Developmental origin provides an important clue for understanding macrophage
282 characteristics. Macrophages in the adult body are supplied via two pathways: primitive
283 macrophages are obtained from erythro-myeloid progenitors (EMPs) in the yolk sac, and
284 during later development, additional macrophages are supplied by hematopoietic stem cells in
285 the bone marrow^{45,46}. Macrophages from different origins exhibit different cellular properties

286 and functions. For example, yolk sac-derived macrophages have higher self-renewal^{45,46} and
287 immunoregulatory^{47,48} properties than bone marrow-derived macrophages. To examine the
288 origin of MP1 and MP2 in the liver, we performed parabiosis experiments using CX₃CR1-
289 tdTomato and wild-type parabionts and revealed that both MP1 and MP2 were hardly replaced
290 by the bone marrow-derived circulating populations for up to 20 weeks. Looking into the small
291 number of replaced tdTomato⁺ macrophages in wild-type parabionts, more than 90 % of these
292 were Marco-negative (**Extended Data Fig. 11a-c**). Also, the bone marrow-derived
293 macrophages did not express TIM-4, a yolk sac-derived resident macrophage
294 marker¹⁹(**Extended Data Fig. 11d**). These results suggest that MP2 is essentially derived from
295 EMPs with high self-renewing capacity and rarely differentiated from hematopoietic stem cells
296 in the bone marrow during the postnatal development. We next deleted the liver resident
297 macrophages with CLL to verify this perspective and analysed the regenerated Kupffer cells
298 after 6 weeks (**Extended Data Fig. 11e-j**). We classified the macrophages using the resident
299 macrophage marker TIM-4 and found that the CLL-treated liver contained survived resident
300 (TIM-4-positive) and bone marrow-derived (TIM-4-negative) populations (**Extended Data**
301 **Fig. 11f-h**). TIM-4⁺ resident macrophages showed greater percentage of Marco-expressing
302 cells and higher expression of *Ii10* mRNA compared to TIM-4⁻ bone marrow-derived
303 macrophages (**Extended Data Fig. 11i, j**). Beattie *et al.* also compared yolk sac-derived
304 Kupffer cells with bone marrow-derived ones by ingeniously creating the chimeric mice. They

305 demonstrated that the bone marrow-derived Kupffer cells did not express Marco, even when
306 stimulated by LPS⁴⁹. The bulk of these results suggests that MP2 should be supplied from
307 EMPs in the yolk sac. Nevertheless, detailed analyses using fate-mapping system are required
308 to elucidate when and how MP1 and MP2 are generated during the liver development.

309 Commensal bacteria and their related pathogens/metabolites that translocate from the gut
310 to the liver contribute to MP2 development in PV zones, which, in turn, suppresses excessive
311 inflammation at the gateway of bacterial entry and maintains homeostasis in the liver. The
312 mechanisms underlying commensal bacteria-induced generation of MP2 remain to be
313 elucidated. However, pattern recognition receptor stimulation by PAMPs or DAMPs in some
314 subpopulations of liver-resident cells, including macrophages (Kupffer cells) and endothelial
315 cells, appears to be involved. In this study, we demonstrated that a specific family of
316 commensals, Odoribacteraceae, enhanced MP2 induction by supplying a characteristic bile
317 acid metabolite, isoallo-LCA. Isoallo-LCA induces structural changes in the chromatin and
318 facilitates DNA binding of transcription factors, particularly the nuclear hormone receptor
319 NR4A1²⁷. In macrophages, NR4A1 plays a critical role in inducing anti-inflammatory
320 properties, such as elevating IL-10 production⁵⁰. Because Kupffer cells also express abundant
321 NR4A1, this molecule may be involved in MP2 differentiation. Additionally, under depleting
322 the gut commensals with antibiotic treatment, oral administration of isoallo-LCA did not induce
323 MP2 (**Extended Data Fig. 7d-f**), suggesting that the interaction of Odoribacteraceae and other

324 bacteria is necessary not only for a sufficient production of isoallo-LCA but also for the
325 induction of MP2 by isoallo-LCA. This is consistent with the present results that
326 *Odoribacteraceae* could enhance the generation of MP2 when co-existence with other
327 commensals under SPF conditions but could not solely induce MP2 (Fig. 4d, e).

328 This study demonstrated the biological significances of the spatially heterogeneous
329 distribution of Kupffer cell subsets with distinct functions. As a gateway from the gut, the liver
330 is inherently vulnerable to external pathogens, and PV zones are prone to inflammation due to
331 biased accumulation of immune cells, especially Kupffer cells^{6,9}. The present results led to a
332 novel concept that the immunomodulatory activity of MP2 in liver PV zones is critical for
333 maintaining healthy conditions against gut commensal infection, and disruption of this
334 protective mechanism may be correlated with intractable liver diseases, such as PSC and
335 NASH. Also, our comprehensive analyses with laboratory animals and human samples
336 demonstrated that MP2 could be a promising target for developing therapeutic approaches
337 against these refractory liver diseases.

338 **Main references**

- 339 1. Jungermann, K. & Kietzmann, T. Zonation of parenchymal and nonparenchymal
340 metabolism in liver. *Annu. Rev. Nutr.* **16**, 179–203 (1996).
- 341 2. Mizukami, K. *et al.* In vivo O₂ imaging in hepatic tissues by phosphorescence lifetime
342 imaging microscopy using Ir(III) complexes as intracellular probes. *Sci. Rep.* **10**, 1–14
343 (2020).
- 344 3. Nauck, M., Wölfle, D., Katz, N. & Jungermann, K. Modulation of the glucagon-
345 dependent induction of phosphoenolpyruvate carboxykinase and tyrosine
346 aminotransferase by arterial and venous oxygen concentrations in hepatocyte cultures.
347 *Eur. J. Biochem.* **119**, 657–661 (1981).
- 348 4. Jungermann, K., Heilbronn, R., Katz, N. & Sasse, D. The glucose/glucose-6-phosphate
349 cycle in the periportal and perivenous zone of rat liver. *Eur. J. Biochem.* **123**, 429–436
350 (1982).
- 351 5. Jungermann, K. & Katz, N. Functional specialization of different hepatocyte populations.
352 *Physiol. Rev.* **69**, 708–764 (1989).
- 353 6. Gola, A. *et al.* Commensal-driven immune zonation of the liver promotes host defence.
354 *Nature* **589**, 131–136 (2021).
- 355 7. Su, T. *et al.* Single-cell transcriptomics reveals zone-specific alterations of liver
356 sinusoidal endothelial cells in cirrhosis. *Cmgh* **11**, 1139–1161 (2021).

- 357 8. Dobie, R. *et al.* Single-cell transcriptomics uncovers zonation of function in the
358 mesenchyme during liver fibrosis. *Cell Rep.* **29**, 1832-1847 (2019).
- 359 9. Guilliams, M. *et al.* Spatial proteogenomics reveals distinct and evolutionarily
360 conserved hepatic macrophage niches. *Cell* **185**, 379-396 (2022).
- 361 10. Halpern, K. B. *et al.* Single-cell spatial reconstruction reveals global division of labour
362 in the mammalian liver. *Nature* **542**, 352–356 (2017).
- 363 11. Dal-Secco, D. *et al.* A dynamic spectrum of monocytes arising from the in situ
364 reprogramming of CCR2⁺ monocytes at a site of sterile injury. *J. Exp. Med.* **212**, 447–
365 456 (2015).
- 366 12. Remmerie, A. *et al.* Osteopontin expression identifies a subset of recruited macrophages
367 distinct from Kupffer cells in the fatty liver. *Immunity* **53**, 641-657 (2020).
- 368 13. Scott, C. L. *et al.* Bone marrow-derived monocytes give rise to self-renewing and fully
369 differentiated Kupffer cells. *Nat. Commun.* **7**, 1–10 (2016).
- 370 14. English, K. *et al.* The liver contains distinct interconnected networks of CX3CR1⁺
371 macrophages, XCR1⁺ type 1 and CD301a⁺ type 2 conventional dendritic cells embedded
372 within portal tracts. *Immunol. Cell Biol.* **100**, 394–408 (2022).
- 373 15. Ramachandran, P. *et al.* Resolving the fibrotic niche of human liver cirrhosis at single-
374 cell level. *Nature* **575**, 512-518 (2019).
- 375 16. MacParland, S. A. *et al.* Single cell RNA sequencing of human liver reveals distinct

- 376 intrahepatic macrophage populations. *Nat. Commun.* **9**, 1–21 (2018).
- 377 17. McDonald, B. *et al.* Intravascular danger signals guide neutrophils to sites of sterile
378 inflammation. *Science* **330**, 362–6 (2010).
- 379 18. Lefort, C. T. & Ley, K. Neutrophil arrest by LFA-1 activation. *Front. Immunol.* **3**, 1–10
380 (2012).
- 381 19. Sakai, M. *et al.* Liver-derived signals sequentially reprogram myeloid enhancers to
382 initiate and maintain Kupffer cell identity. *Immunity* **51**, 655–670 (2019).
- 383 20. Shichita, T. *et al.* MAFB prevents excess inflammation after ischemic stroke by
384 accelerating clearance of damage signals through MSR1. *Nat. Med.* **23**, 723–732 (2017).
- 385 21. Andersson, L. & Freeman, M. W. Functional changes in scavenger receptor binding
386 conformation are induced by charge mutants spanning the entire collagen domain. *J.*
387 *Biol. Chem.* **273**, 19592–19601 (1998).
- 388 22. Ojala, J. R. M., Pikkarainen, T., Tuuttila, A., Sandalova, T. & Tryggvason, K. Crystal
389 structure of the cysteine-rich domain of scavenger receptor MARCO reveals the
390 presence of a basic and an acidic cluster that both contribute to ligand recognition. *J.*
391 *Biol. Chem.* **282**, 16654–16666 (2007).
- 392 23. Mukhopadhyay, S. *et al.* SR-A/MARCO-mediated ligand delivery enhances
393 intracellular TLR and NLR function, but ligand scavenging from cell surface limits
394 TLR4 response to pathogens. *Blood* **117**, 1319–1328 (2011).

- 395 24. Jing, J. *et al.* Role of macrophage receptor with collagenous structure in innate immune
396 tolerance. *J. Immunol.* **190**, 6360–6367 (2013).
- 397 25. Leinwand, J. C. *et al.* Intrahepatic microbes govern liver immunity by programming
398 NKT cells. *J. Clin. Invest.* **132**, e151725 (2022).
- 399 26. Sato, Y. *et al.* Novel bile acid biosynthetic pathways are enriched in the microbiome of
400 centenarians. *Nature* **599**, 458–464 (2021).
- 401 27. Li, W. *et al.* A bacterial bile acid metabolite modulates Treg activity through the nuclear
402 hormone receptor NR4A1. *Cell Host Microbe* **29**, 1366–1377 (2021).
- 403 28. Spadoni, I. *et al.* A gut-vascular barrier controls the systemic dissemination of bacteria.
404 *Science* **350**, 830–834 (2015).
- 405 29. Sookoian, S. *et al.* Intrahepatic bacterial metataxonomic signature in non-alcoholic fatty
406 liver disease. *Gut* **69**, 1483–1491 (2020).
- 407 30. Luther, J. *et al.* Hepatic injury in nonalcoholic steatohepatitis contributes to altered
408 intestinal permeability. *Cell. Mol. Gastroenterol. Hepatol.* **1**, 222–232 (2015).
- 409 31. Manfredo Vieira, S. *et al.* Translocation of a gut pathobiont drives autoimmunity in mice
410 and humans. *Science* **360**, 1156–1161 (2018).
- 411 32. Nakamoto, N. *et al.* Gut pathobionts underlie intestinal barrier dysfunction and liver T
412 helper 17 cell immune response in primary sclerosing cholangitis. *Nat. Microbiol.* **4**,
413 492–503 (2019).

- 414 33. Thaiss, C. A. *et al.* Hyperglycemia drives intestinal barrier dysfunction and risk for
415 enteric infection. *Science* **359**, 1376–1383 (2018).
- 416 34. Lazaridis, K. N. & LaRusso, N. F. Primary sclerosing cholangitis. *N. Engl. J. Med.* **375**,
417 1161–1170 (2016).
- 418 35. Dyson, J. K., Beuers, U., Jones, D. E. J., Lohse, A. W. & Hudson, M. Primary sclerosing
419 cholangitis. *Lancet* **391**, 2547–2559 (2018).
- 420 36. Horsley-Silva, J. L., Carey, E. J. & Lindor, K. D. Advances in primary sclerosing
421 cholangitis. *Lancet Gastroenterol. Hepatol.* **1**, 68–77 (2016).
- 422 37. O’Toole, A. *et al.* Primary sclerosing cholangitis and disease distribution in
423 inflammatory bowel disease. *Clin. Gastroenterol. Hepatol.* **10**, 439–441 (2012).
- 424 38. Matteoni, C. A. *et al.* Nonalcoholic fatty liver disease: A spectrum of clinical and
425 pathological severity. *Gastroenterology* **116**, 1413–1419 (1999).
- 426 39. Bouwens, L., Baekeland, M., De Zanger, R. & Wisse, E. Quantitation, tissue distribution
427 and proliferation kinetics of Kupffer cells in normal rat liver. *Hepatology* **6**, 718–22
428 (1986).
- 429 40. Knoll, P. *et al.* Human Kupffer cells secrete IL-10 in response to lipopolysaccharide
430 (LPS) challenge. *J. Hepatol.* **22**, 226–229 (1995).
- 431 41. Balmer, M. L. *et al.* The liver may act as a firewall mediating mutualism between the
432 host and its gut commensal microbiota. *Sci. Transl. Med.* **6**, 237ra66 (2014).

- 433 42. van der Laan, L. J. *et al.* Regulation and functional involvement of macrophage
434 scavenger receptor MARCO in clearance of bacteria in vivo. *J. Immunol.* **162**, 939–47
435 (1999).
- 436 43. Blériot, C. *et al.* A subset of Kupffer cells regulates metabolism through the expression
437 of CD36. *Immunity* **54**, 2101-2116 (2021).
- 438 44. De Simone, G. *et al.* Identification of a Kupffer cell subset capable of reverting the T
439 cell dysfunction induced by hepatocellular priming. *Immunity* **54**, 2089-2100 (2021).
- 440 45. Yona, S. *et al.* Fate mapping reveals origins and dynamics of monocytes and tissue
441 macrophages under homeostasis. *Immunity* **38**, 1073–1079 (2013).
- 442 46. Liu, Z. *et al.* Fate mapping via Ms4a3-expression history traces monocyte-derived cells.
443 *Cell* **178**, 1509-1525 (2019).
- 444 47. van de Laar, L. *et al.* Yolk sac macrophages, fetal liver, and adult monocytes can
445 colonize an empty niche and develop into functional tissue-resident macrophages.
446 *Immunity* **44**, 755–768 (2016).
- 447 48. Tran, S. *et al.* Impaired Kupffer cell self-renewal alters the liver response to lipid
448 overload during non-alcoholic steatohepatitis. *Immunity* **53**, 627-640 (2020).
- 449 49. Beattie, L. *et al.* Bone marrow-derived and resident liver macrophages display unique
450 transcriptomic signatures but similar biological functions. *J. Hepatol.* **65**, 758–768
451 (2016).

452 50. Koenis, D. S. *et al.* Nuclear Receptor Nur77 Limits the Macrophage Inflammatory
453 Response through Transcriptional Reprogramming of Mitochondrial Metabolism. *Cell*
454 *Rep.* **24**, 2127-2140 (2018).

455

456 **Figure Legends**

457

458 **Fig. 1. A periportal macrophage subset suppressively regulates periportal immune**

459 **activation. a**, Spatial transcriptomics showing hepatic zonation (n = 4): gene expression of

460 *Cyp2f2* (left-upper) and *Cyp2e1* (left-lower), identified zones (right-upper, blue: PV zones,

461 orange: CV zones, green: marginal zones), and H&E staining (right-lower). **b**, Immune

462 pathways enriched in PV zones (vs. CV zones). P-values were determined using one-sided

463 Fisher's exact test. **c**, Representative intravital images of in situ inflammatory responses of

464 neutrophils against sterile laser-induced damages in control (**top**) and macrophage-depleted

465 mice (**bottom**) [n = 14 each, green: neutrophils, white: damaged sites (**autofluorescence**), and

466 blue: collagens visualised using second harmonic generation (SHG)]. Scale bar: 100 μ m. **d**,

467 Neutrophil accumulation scores in control (left) and macrophage-depleted mice (right). Data

468 are presented as means \pm standard error of the mean (SEM). P-value was determined using

469 paired two-sided Mann–Whitney U test at 3 h. **e**, Schematics of isolation of zone-specifically

470 labelled immune cells. Scale bar: 50 μ m. **f**, t-Distributed Stochastic Neighbour Embedding

471 (tSNE) plot depicting each immune cell cluster and location (left). The localisation score

472 (PV/CV ratio) (right). **g**, Expression of *Clec4f* and *Marco* shown on the tSNE plot. **h**, Violin

473 plots depicting expression of the anti-inflammatory cytokines *Il10*, *Il1rn*, and *Tgfb1* in MP1

474 and MP2. **Statistical significance was determined using a two-sided Wilcoxon Rank Sum test.**

475 **i**, Representative immunofluorescence image showing Marco (green), F4/80 (red), and E-
476 cadherin (blue) (left, n = 4, 33 visual fields). Localisation score (PV/CV ratio) of Marco⁺ and
477 Marco⁻ macrophages (right). Scale bar: 100 μm. Data are presented as means (asterisk) with
478 medians, smallest observations, lower and upper quartiles, and largest observations. Statistical
479 significance was determined using unpaired two-sided Mann–Whitney U test. The exact *p*-
480 value is 2.2×10^{-16} .

481

482 **Fig. 2. The Marco–IL-10 axis is necessary for establishing an immunosuppressive niche**

483 **in periportal regions. a,** mRNA expression of *Il10* in MP2 and other immune cell types

484 identified in the single-cell transcriptomics. Statistical significance was determined using a

485 two-sided Wilcoxon Rank Sum test. The *p*-value was adjusted based on Bonferroni correction.

486 **b,** Relative mRNA expression of *Il10* to *Gapdh* in MP2 (n = 6), LSECs (n = 8), HSCs (n = 7),

487 and hepatocytes (n = 6). **c,** Representative intravital images of in situ inflammatory responses

488 of neutrophils upon laser-induced tissue damages under treatment with isotype control antibody

489 (left) and anti-IL-10R antibody (centre) [n = 6 per condition, green: neutrophils, white:

490 damaged sites (autofluorescence), and blue: SHG (tissue collagens)]. Scale bar: 100 μm.

491 Spatially biased neutrophil accumulation at 3 h post-laser ablation is shown as the PV/CV ratio

492 (right). **d,** Representative intravital images of in situ inflammatory responses of neutrophils

493 upon laser-induced tissue damages in *Marco*^{+/+} wild-type (left, n = 10) and *Marco*^{-/-} knockout

494 (centre, n = 7) mice [green: neutrophils, white: damaged sites, and blue: SHG (tissue

495 collagens)]. Scale bar: 100 μm. Spatially biased neutrophil accumulation at 3 h post-laser

496 ablation is shown as the PV/CV ratio (right). All quantitative data are presented as means

497 (asterisk) with medians, smallest observations, lower and upper quartiles, and largest

498 observations. Statistical significance was determined using unpaired two-sided Mann–Whitney

499 U test.

500

501 **Fig. 3. Gut commensal microbes induce the periportal immunosuppressive Kupffer cells.**

502 **a**, Representative immunofluorescence images showing Marco (green), F4/80 (red), and E-

503 cadherin (blue) in liver sections from specific pathogen-free (SPF, n = 11, 35 visual fields),

504 germ-free (GF, n = 5, 27 visual fields), antibiotic-treated (ABX, n = 9, 26 visual fields), and

505 MyD88 knockout mice (*MyD88*^{-/-}, n = 5, 39 visual fields). Scale bar: 100 μm. **b**, Absolute

506 number of F4/80-positive cells (total Kupffer cells) per visual field. **c**, Percentage of Marco⁺

507 **immunosuppressive** Kupffer cells (MP2) to total Kupffer cells quantified using flow cytometry.

508 **d,e**, Relative mRNA expression of *Il10* to *Gapdh* in total Kupffer cell fractions (d) and tissue

509 lysates (e) from SPF control (n = 9) and ABX (n = 7) mice. **f**, Representative intravital images

510 of in situ inflammatory responses of neutrophils upon laser-induced damage in control (left, n

511 = 10) and ABX (centre, n = 12) mice [green: neutrophils, white: damaged sites, and blue: SHG

512 (tissue collagens)]. Scale bar: 100 μm. Spatially biased neutrophil accumulation at 3 h post-

513 laser ablation is shown as the PV/CV ratio (right). All quantitative data are presented as means

514 (asterisk) with medians, smallest observations, lower and upper quartiles, and largest

515 observations. Statistical significance was determined using unpaired two-sided Mann–Whitney

516 U test.

517

518 **Fig. 4. Odoribacteraceae promotes induction of the periportal immunosuppressive**

519 **Kupffer cells by providing isoallo-lithocholic acids. a, Percentage of Marco⁺**

520 **immunosuppressive** Kupffer cells (MP2) to total Kupffer cells from SPF-A and SPF-B mice.

521 **b, Relative abundance (%) of Odoribacteraceae in colorectal contents from SPF-A and SPF-B**

522 **mice. c, Correlation between the abundance of Odoribacteraceae and the percentage of MP2.**

523 **'R'** indicates the correlation coefficient. **d, Graphical protocol for generating gnotobiotic mice**

524 **(left). Odori and Stercoris indicate Odoribacteraceae and *B. Stercoris*, respectively. Percentage**

525 **of MP2 to total Kupffer cells (right). e, Graphical protocol for generating symbiotic conditions**

526 **of target and SPF microbes (left). Sterile PBS-inoculated GF mice were used as a negative**

527 **control. Percentage of MP2 to total Kupffer cells (right). f, Concentration of isoallo-lithocholic**

528 **acid (isoallo-LCA) in faeces. g, Graphical protocol for oral administration of isoallo-LCA or**

529 **the vehicle control, dimethyl sulfoxide (DMSO) (left). Percentage of MP2 to total Kupffer cells**

530 **(right). h, Fold changes of *Il10* mRNA expression in Kupffer cells. Data were standardized to**

531 **ensure a control group mean value of '1'. All quantitative data are presented as means (asterisk)**

532 **with medians, smallest observations, lower and upper quartiles, and largest observations.**

533 **Statistical significance was determined using unpaired two-sided Mann–Whitney U test.**

534

535 **Fig. 5. Periportal immunosuppressive Kupffer cells protect against gut bacteria-driven**
536 **inflammation. a**, Experimental design of chronic colitis-induced liver inflammation. **b**, The
537 heatmap representing fold changes of each immune cell type against the healthy control. **c**,
538 Absolute numbers of CD45-positive cells, neutrophils, and Th17 cells from DSS-treated
539 *Marco*^{+/+} (n = 12) and *Marco*^{-/-} (n = 11) mice. **d**, Representative intravital images of infiltrating
540 LysM-GFP⁺ cells, including neutrophils/macrophages, in DSS-treated *Marco*^{+/+} and *Marco*^{-/-}
541 mice on day 39 [n = 3 per condition, green: LysM-GFP⁺ cells, blue: SHG (tissue collagens)].
542 Scale bar: 100 μm. PV, portal vein; CV, central vein. **e**, Serum ALT and AST levels from DSS-
543 treated *Marco*^{+/+} (n = 14) and *Marco*^{-/-} (n = 16) mice. **f**, Relative mRNA expression of fibrosis
544 markers *Timp1* (left) and *Coll1a1* (right) to *Gapdh* in tissue lysates from DSS-treated *Marco*^{+/+}
545 (n = 12) and *Marco*^{-/-} (n = 11) mice. **g**, Representative immunofluorescence images are shown
546 (left). Scale bar: 100 μm. Quantification of type I collagen accumulations in PV zones:
547 *Marco*^{+/+} (n = 6, 12 visual fields) and *Marco*^{-/-} (n = 7, 14 visual fields). **h**, Representative
548 immunofluorescence images showing MARCO (green), CD68 (red), and CK19 (cyan) in
549 human livers: PSC (n = 6, 18 visual fields) and normal controls (n = 9, 27 visual fields). Scale
550 bar: 100 μm. **i**, Quantified information: the absolute numbers of CD68-positive cells
551 (macrophages) per visual field (left). Percentage of *Marco*⁺ cells to total macrophages in visual
552 fields (centre). The exact *p*-value is 1.166×10^{-12} . Percentage of periportal *Marco*⁺

553 macrophages within 200 μm from bile ducts (right). The exact p -value is 1.92×10^{-8} . All
554 quantitative data are presented as means (asterisk) with medians, smallest observations, lower
555 quartiles, upper quartiles, and largest observations. Statistical significance was determined
556 using unpaired two-sided Mann–Whitney U test.

557 **Methods**

558 **Mice**

559 C57BL/6 wild-type and germ-free mice were purchased from CLEA Japan, Inc. *Myd88*^{-/-51}
560 mice were purchased from Oriental Bio Service, Inc. Photoactivatable-GFP (PA-GFP)⁵² mice
561 were provided by Dr. Michel Nussenzweig (Rockefeller University). Rosa-tdTomato (Ai9)⁵³
562 and Cx3cr1-Cre⁴⁵ mice were purchased from the Jackson Laboratory. Generation of
563 *Marco*^{-/-54}, *Il10*-Venus⁵⁵, LysM-GFP⁵⁶, and CX₃CR1-GFP⁵⁷ mice has been described
564 previously. This study used 8–20-week-old female or male mice (no sex difference was
565 confirmed). All mice were randomly housed in groups and selected for the experiments. Mice
566 were fed a normal diet (MF diet; Oriental Yeast Co., Ltd.) and maintained at 23 ± 1.5 °C and
567 45 ± 15% relative humidity under a 12 h/12 h light/dark cycle in specific pathogen-free animal
568 facilities at Osaka University. All animal experiments were approved by the Institutional
569 Animal Experimental Committee of Osaka University.

570

571 **Parabiosis**

572 Transgenic mice (Rosa-LSL-tdTomato:Cx3cr1-Cre) were surgically connected to wild-type
573 mice as described previously⁵⁸. Briefly, the lateral skin incisions were made from the elbow to
574 the knee in each mouse, and then the forelimbs and hind limbs were tied together using silk
575 sutures. We made approximately 1 cm incisions in the peritoneum of each mouse, and the mice

576 were attached them using silk sutures. The skin incisions were closed using stainless steel
577 wound clips.

578

579 **Drug treatment**

580 To deplete Kupffer cells, we used clodronate liposome according to a previous study⁵⁹. Briefly,
581 500 µg clodronate liposome (#MKV100, Cosmo Bio) in 200 µL phosphate-buffered saline
582 (PBS) was intravenously injected via the tail vein (**Fig.1, Extended Data Fig.2,**
583 **Supplementary Fig. 1**) and 650 µg clodronate liposome in 200 µL PBS was injected in the
584 same way (**Extended Data Fig. 11**). The mice were used for further experiments 2 days later
585 (**Fig.1, Extended Data Fig.2, Supplementary Fig. 1**) and 6 weeks later (**Extended Data Fig.**
586 **11**), respectively. To examine the effects of in vivo blockade of IL-10 signalling, we used an
587 anti-IL-10R antibody based on the method of a previous study⁶⁰. Briefly, 200 µg anti-IL-10R
588 antibody (#112710, BioLegend) or rat IgG1,κ antibody (#400432, BioLegend) as isotype
589 control was intraperitoneally injected every 2 days for 5 days, and the mice were used for the
590 experiments on day 5. To assess MP2 induction by isoallo-lithocholic acid (isoallo-LCA)
591 treatment, we administered 200 µg of isoallo-LCA (#29542, Cayman) via oral gavage. Prior to
592 the administration, 10 mg/mL isoallo-LCA in DMSO was prepared as a stock solution and
593 stored at -80 °C before use. From this stock, 1 mg/mL isoallo-LCA solution was prepared by
594 diluting 10 times with PBS, and 200 µL was administered daily for 2 weeks. As a control, 10%

595 (v/v) DMSO in PBS was administered similarly. To deplete the gut commensals, we treated
596 mice with antibiotics, similar to a previous study⁶¹. Briefly, 8-week-old mice received 1 g/L
597 ampicillin sodium (#19769-64, Nacalai), 0.5 g/L vancomycin hydrochloride (#36137-91,
598 Nacalai), 1 g/L neomycin sulphate (#19767-84, Nacalai), and 1 g/L metronidazole (#23254-64,
599 Nacalai) in their drinking water for 6 weeks (**Fig. 3 and 4**). The antibiotic-containing water
600 was replaced with a fresh one every 4 days. In **Extended Data Fig. 7d-f**, mice received the
601 same antibiotic-containing water for 1 week, following half the concentration of the complete
602 antibiotic-containing water for 2 weeks during the isoallo-LCA treatment.

603

604 **Spatial transcriptome analysis using Visium™**

605 The mice were euthanised via CO₂ overdose. The liver was immediately excised, and each
606 liver lobe was embedded in Tissue-Tek O.C.T. Compound (Sakura) and snap-frozen in
607 isopentane (Sigma) chilled by liquid nitrogen. The frozen tissue blocks were sliced into 10 µm
608 sections and placed within the capture area of a 10× Visium Spatial Gene expression slide (10×
609 Genomics). The 10x Visium cDNA library was prepared according to the manufacturer's
610 instructions. cDNA libraries from four samples were sequenced on a NovaSeq 6000 (Illumina,
611 USA) platform in a 28+120-base paired-end mode.

612 The raw sequenced reads were processed using 10× Genomics CellRanger 1.0.0. The four
613 sample data were merged to account for the batch effect between samples using Scanorama⁶²

614 and Scanpy⁶³. The expression levels of the hepatic zonation markers *Cyp2f2* and *Cyp2e1*¹⁰ were
615 used to classify the Visium spots into portal vein (PV) and central vein (CV) zones. Briefly, the
616 expression levels of *Cyp2f2* and *Cyp2e1* exhibited a bimodal distribution, and the distributions
617 were fitted for each gene using a ‘two-component mixed Gaussian model’ (**Supplementary**
618 **Fig. 6**). Establishing a threshold at the junction of the high and low expression distributions
619 should provide a suitable criterion for zonal classification. Visium spots with higher expression
620 of *Cyp2f2* and lower expression of *Cyp2e1* compared with the threshold were defined as PV
621 zones. In contrast, spots with higher expression of *Cyp2e1* and lower expression of *Cyp2f2*
622 compared with the threshold were defined as CV zones. Subsequently, we examined the
623 differentially expressed genes (DEGs) in each zone by statistically comparing the gene
624 expression levels between the identified PV and CV zones with ‘Rank genes for characterizing
625 groups’ function implemented in Scanpy, and extracted 630 and 340 DEGs, which were
626 enriched in PV and CV zones, respectively. Genes showing adjusted *P*-values (Benjamini-
627 Hochberg method) of more than 0.05 were excluded. We then performed the Gene Ontology
628 analysis using the periportally enriched 630 genes with the software DAVID⁶⁴ (version 6.8)
629 and extracted the terms (biological pathways), which contain immune-related genes and show
630 $P < 0.05$.

631

632 **Intravital imaging of the liver and induction of inflammatory immune responses**

633 All surgical procedures in mice were conducted under anaesthesia with isoflurane (#099-
634 06571, Wako). The left lobe of the liver was surgically exposed and gently placed on a cover
635 glass fixed on the imaging stage. The treated mouse was placed in an environmental dark box
636 and warmed to 37°C by an air heater. The internal surface of the liver was observed using an
637 inverted two-photon excitation microscope (A1R-MP, Nikon, Japan) driven by a laser
638 (Chameleon Vision Ti; Sapphire, Coherent) tuned to 870 nm, with a ×20 water immersion
639 objective lens (CFI LWD Lambda S WI, numerical aperture: 0.95, Nikon). Emission
640 wavelengths were detected via bandpass emission filters at 492/SP nm for the second harmonic
641 generation, 525/50 nm for GFP, 575/25 nm for autofluorescence, and 629/56 nm for
642 Qtracker655. This microscopy system was operated using NIS elements software (Nikon).
643 Qtracker655 Vascular Labels (#Q21021MP, Invitrogen) were diluted 20 times in phosphate-
644 buffered saline (PBS) (#14249-95, Nacalai), and 50 µL of the diluted Qtracker655 Vascular
645 Labels was rapidly administered intravenously through a peripheral intravenous line under
646 imaging to detect the PV and CV zones (**Supplementary Video 9**). Image stacks were collected
647 at 3-µm vertical steps up to a depth of 48 µm below the liver surface at an X–Y resolution of
648 512 × 512 pixels (1.24 µm/pixel). Raw imaging data were processed using NIS elements
649 (Nikon) and ImageJ software⁶⁵. Two-dimensional maximum-intensity projection (MIP) images
650 were generated using NIS elements. Background subtraction, median filtering, and binarization
651 were performed using ImageJ. The accumulation score was measured as the integrated area of

652 binarized cells within the region of interest. All images and videos are displayed as MIP images.

653 To activate local immune cells, we induced necrotic tissue damages measuring $< 20 \mu\text{m}$ using
654 infrared laser pulses within PV and CV zones, at $10\text{--}20 \mu\text{m}$ away from each blood vessel and
655 below the liver capsule, based on the methods of previous studies with minor modifications^{66,67}.
656 Intravital imaging commenced immediately after the laser ablation and was performed for 3 h
657 at a time resolution of 30 **sec** to track the neutrophil movements. Additionally, to observe
658 monocyte/macrophage dynamics, we induced the thermal damages in the liver, and then re-
659 introduced the liver lobe into the mouse body and closed the peritoneum and skin incisions
660 using silk sutures. The mouse was allowed free movement for 24 hours. Monocyte/macrophage
661 accumulation at the damage sites was recorded 24 h post laser ablation (**Extended Data Fig.**
662 **2b**).

663

664 **Zone-specific isolation of leukocytes from the liver**

665 To demarcate the PV zones, we intravenously injected $2 \mu\text{g}$ of **phycoerythrin (PE)**-conjugated
666 anti-E-cadherin antibody (#147304, BioLegend) in $200 \mu\text{L}$ PBS into a PA-GFP mouse. After
667 20 min, the liver was harvested, and fresh tissue sections ($250 \mu\text{m}$ thickness) were cut using a
668 Vibratome (Leica, Germany) in chilled HBSS (#17461-05, Nacalai) containing 25 mM HEPES
669 (#15630080, Gibco) and 2% foetal bovine serum (FBS) (Lot:12B247, Sigma). The sections
670 were placed on glass-bottom dishes (#627860, Greiner) and then covered with absorbent cotton

671 soaked with a cold buffer. The subsequent procedures were performed in the cooled equipment.
672 Photoactivation in PV or CV zones was performed using a single-photon 405 nm violet laser
673 while observing the sections under a two-photon excitation microscope (A1R-MP, Nikon)^{52,68}.
674 The photoactivated sections were digested in RPMI medium (#61870036, Gibco) containing
675 10 mM HEPES, 0.033 mg/mL Liberase (#5401119001, Roche), 0.05 mg/mL DNase
676 (#LS002139, Worthington), and 0.35 mM CaCl₂ (#036-19731, Wako) for 35 min with agitation.
677 The single-cell suspension was filtered through a 100 µm cell strainer, and the undigested
678 material was mashed through a 100 µm cell strainer before centrifugation at 500 × g for 5 min.
679 The supernatant was discarded, and the pellet was resuspended in 100 µL PBS, followed by
680 the addition of 0.2 µL Zombie NIR solution (#423105, BioLegend), and then the samples were
681 incubated for 15 min at room temperature (RT, approximately 25 °C) to stain dead cells. Finally,
682 400 µL autoMACS running buffer (#130-091-221, Miltenyi) was added before fluorescence-
683 activated cell sorting (FACS) staining.

684

685 **Unbiased isolation of leukocytes from the liver**

686 Liver leukocytes were isolated as described previously¹⁵, with slight modifications. Briefly,
687 the livers were minced into smaller pieces using scissors and then digested in RPMI medium
688 containing 0.625 mg/mL collagenase D (#11088858001, Roche), 0.85 mg/mL collagenase V
689 (#C9263, Sigma), 1 mg/mL dispase (#17105041, Gibco), and 30 U/mL DNase (#10104159001,

690 Roche) for 20 min with agitation at 37 °C. All the subsequent procedures were conducted at
691 4 °C. The single-cell suspension was filtered through a 100 µm cell strainer, and undigested
692 pieces were mashed through a 100 µm cell strainer before centrifuging at 500 × g for 5 min.
693 The supernatant was discarded, and the pellet was resuspended in 5 mL RPMI containing 2%
694 FBS. The cell suspension was added on 5 mL 33% Percoll (#17089102, GE) in a 15-mL Falcon
695 tube, and centrifuged at 800 × g for 20 min at 20 °C. Next, the top 5.5 mL was aspirated and
696 discarded, and the remainder was washed in additional PBS and centrifuged at 500 × g for 5
697 min. The resulting supernatant was discarded, and the pellet was resuspended in ACK lysis
698 buffer (#A1049201, Gibco) for 3 min to remove red blood cells. The cell suspensions were
699 then washed in PBS containing 2% FBS, filtered through a 70 µm cell strainer, and centrifuged
700 at 500 × g for 5 min. The pellet was resuspended in autoMACS running buffer before FACS
701 staining.

702

703 **Isolation of hepatocytes, liver sinusoidal endothelial cells (LSECs), and hepatic stellate**
704 **cells (HSCs)**

705 Hepatocytes, LSECs, and HSCs were isolated as described previously⁶⁹. Briefly, the livers
706 were perfused with EGTA (#E3889, Sigma) solution and 0.2 mg/mL collagenase A
707 (#10103578001, Roche) solution at a flow rate of 6 mL/min. The livers were mashed through
708 a 100 µm cell strainer and incubated in RPMI medium containing 25 mM HEPES, 0.4 mg/mL

709 collagenase A, and 10 U/mL DNaseI (#10104159001, Roche) for 20 min with agitation at 37°C.
710 After filtration through a 100 µm cell strainer, the cell suspensions were centrifuged at 400 ×
711 g for 7 min and resuspended in ACK lysis buffer for 3 min to remove red blood cells. The cell
712 suspensions were washed in PBS containing 2% FBS and filtered through a 100 µm cell strainer.
713 The cell suspensions were centrifuged at 50 × g for 1 min to segregate the cell fractions as
714 follows; the pellet and supernatant were collected as the hepatocyte fraction and
715 leukocyte/LSEC/HSC fraction, respectively. This procedure was repeated three times. Both
716 fractions were centrifuged at 400 × g for 7 min before FACS staining.

717

718 **Flow cytometry and cell sorting**

719 Cell-surface Fc receptors were blocked in anti-mouse CD16/32 antibody (1:250, #553141, BD
720 Bioscience) for 20 min at 4 °C before staining with FACS antibodies. Subsequently, the primary
721 antibodies were added. All antibodies, conjugates, lot numbers and dilution rates are listed in
722 **Supplementary Table 1**. For Marco staining, cells were stained with a primary unconjugated
723 antibody, followed by staining with a fluorophore-conjugated secondary antibody. The cells
724 were incubated for 30 min at 4°C for staining, followed by washing in PBS containing 2% FBS.
725 After centrifugation at 500 × g for 5 min, the cells were resuspended in autoMACS running
726 buffer. For intracellular cytokine staining, cells were stimulated for 5 h with 50 ng/mL phorbol
727 12-myristate 13-acetate (Sigma-Aldrich) and 500 ng/mL ionomycin (Sigma-Aldrich) in the

728 presence of 10 µg/mL Golgistop (BD Bioscience). Cell surface markers were stained first. After
729 washing with 2% FBS-containing PBS, fixation and permeabilisation were performed using an
730 Intracellular Fixation and Permeabilisation Buffer set (eBioscience™), followed by
731 intracellular cytokine staining. The cells were resuspended in autoMACS running buffer. Raw
732 data were obtained using FACS Celesta (BD Biosciences, USA) or SH800 cell sorter (Sony,
733 Japan) and analysed using FlowJo (BD Biosciences). Cell sorting was performed on the SH800
734 cell sorter. Gating strategies are shown in **Supplementary Fig. 7**.

735

736 **Single-cell RNA sequencing**

737 The 10× Genomics Chromium Controller was used to construct a single-cell RNA library and
738 sequence the single-cell suspension following the protocol outlined in the Chromium Single
739 Cell 3' Reagent Kit User Guide. We used the Chromium Next GEM Single Cell 3' Kit v3.1
740 (#PN-1000269; 10x Genomics), Chromium Next GEM Chip G Single Cell Kit (#PN-1000127;
741 10x Genomics), and Dual Index Kit TT Set A (#PN-1000215; 10× Genomics). According to
742 the manufacturer's recommendations, approximately 2,000 live cells per sample were loaded
743 onto the Chromium controller to generate 2,000 single-cell gel-bead emulsions for library
744 preparation and sequencing. Oil droplets of encapsulated single cells and barcoded beads
745 (GEMs) were subsequently reverse-transcribed in the Veriti Thermal Cycler (Thermo Fisher
746 Scientific), resulting in cDNA tagged with a cell barcode and unique molecular index. Next,

747 cDNA was amplified to generate single-cell libraries according to the manufacturer's protocol.
748 The Agilent Bioanalyzer High Sensitivity DNA assay (#5067-4626; Agilent) was used to
749 quantify the cDNA before it was enzymatically fragmented, end-repaired, and polyA-tagged.
750 Cleanup/size selection was performed on the amplified cDNA using SPRIselect magnetic beads
751 (#B23317, Beckman-Coulter). Next, Illumina sequencing adapters were ligated to the size-
752 selected fragments and purified using SPRIselect magnetic beads. Finally, sample indices were
753 selected and amplified, followed by double-sided size selection using SPRIselect magnetic
754 beads. The final library quality was assessed using the Agilent Bioanalyser High Sensitivity
755 DNA assay. The samples were then sequenced on the Illumina NovaSeq 6000 in paired-end
756 mode (read 1: 28 bp; read 2: 91 bp). The resulting raw reads were processed using 10×
757 Genomics CellRanger 4.0.0.

758

759 **Processing of single-cell RNA sequencing data**

760 R (version 4.1.2) and Seurat (version 4.1.1) were used for processing the single-cell
761 transcriptome data⁷⁰. Unsupervised clustering and gene expression analysis were performed
762 according to the Seurat guidance. In brief, we omitted the genes and cells in the data based on
763 the following criteria: (1) the genes detected in fewer than five cells, (2) the cells with fewer
764 than 200 or more than 5,000 genes, and (3) the cells with more than 20% mitochondrial genes.
765 In mouse zone-specific single-cell RNA-seq, a total of 2,461 cells (including 1,282 cells and

766 1,179 cells from PV and CV zones, respectively) were selected for the subsequent analysis. In
767 a reanalysis of public human single-cell data, a total of 28,609 cells (including 16,786 and
768 11,823 cells from healthy and cirrhotic samples, respectively) were selected for the subsequent
769 analysis. Multiple data were integrated using the reciprocal principal components analysis
770 (RPCA)-based integration method, then linear dimensional reduction was performed using a
771 principal component analysis method. Cluster classification was performed using the nearest
772 neighbour graph-based clustering method, in which we tuned the dimensionality and resolution
773 parameters to determine the number of clusters. In the mouse analysis, 14 cell clusters were
774 initially obtained by setting the dimensionality to “1:15” and the resolution to “0.42.” In the
775 human analysis, 14 cell clusters were initially obtained by setting the dimensionality to “1:15”
776 and the resolution to “0.2.” Subsequently, we searched for marker genes for each cluster using
777 a ‘FindAllMarkers’ function and assign clusters to known cell types based on the markers
778 (**Supplementary Tables 2 and 3**) with reference to the previous reports^{9,12,15,16,71–73}; however,
779 we omitted clusters that could not be assigned.

780

781 **Quantitative reverse transcription-polymerase chain reaction (qRT-PCR)**

782 Total RNA was extracted and purified using the RNeasy mini kit (#74106, Qiagen). cDNA was
783 prepared using Superscript III reverse transcriptase (#18080044, Invitrogen) following the
784 manufacturer’s instructions. Real-time PCR was performed using TB Green Premix EX Taq

785 (#RR420W, TaKaRa) on a Thermal Cycler Dice Real Time System (TaKaRa, Japan). Relative
786 gene expression levels were calculated by the $\Delta\Delta\text{Ct}$ method using *Gapdh* as an internal control.
787 The specific primer pairs (forward and reverse sequences, respectively) are listed in
788 **Supplementary Table 4**. *Gapdh* is a broadly acceptable choice as one of the stable
789 housekeeping genes for use in macrophages⁷⁴. We also confirmed the validity of *Gapdh* by
790 comparing the results with that of other commonly used internal control genes, *18s*, *Rpl32*,
791 *B2m*, and *Ubc* (the data are shown in **Supplementary Fig. 8**). Furthermore, we validated the
792 accuracy of the qPCR results by conducting a multimodal analysis.

793

794 **Immunofluorescence staining and confocal imaging**

795 The livers were embedded in 4% paraformaldehyde (PFA) (#158127, Sigma) solution
796 overnight and then dehydrated using 15% and 30% sucrose solutions. The livers were cut into
797 small pieces and embedded in Tissue-Tek O.C.T.TM Compound. Frozen sections (20 μm
798 thickness) were cut using a CM3050S cryostat (Leica) and fixed on APS-coated slides
799 (Matsunami). The sections were permeabilised in 0.5% tween-20 (#P1379, Sigma) solution for
800 20 min at RT and blocked in 4% bovine serum albumin (BSA) (#A6003, Sigma) solution for
801 60 min. Subsequently, the sections were stained with antibodies diluted in PBS containing 0.1%
802 tween-20 and 1% BSA. The antibodies used for tissue staining are listed in **Supplementary**
803 **Table 1**. After staining, the slides were mounted in PBS and scanned on a confocal microscope

804 (A1R, Nikon) with a $\times 20$ objective lens (CFI Plan Apo VC, numerical aperture: 0.75, Nikon).
805 Raw imaging data were processed using NIS elements (Nikon) and Imaris (Bitplane). Cell
806 counting and cellular morphological analysis were performed using Imaris with the Spot and
807 Surface functions, respectively.

808

809 **16S rRNA-sequencing of colorectal bacteria**

810 Colorectal contents were squeezed out from just below the cecum to the anus. The samples
811 were instantly frozen with liquid nitrogen. DNA was extracted from the samples using GENE
812 PREP STAR PI-1200 (Kurabo, Japan) according to the manufacturer's protocol. Each library
813 was prepared according to the Illumina 16S Metagenomic Sequencing Library Preparation
814 Guide with the primer set, 27Fmod: 5'AGRGTTCGATCMTGGCTCAG-3' and 338R: 5'-
815 TGCTGCCTCCCGTAGGAGT-3', targeting the V1–V2 regions of the 16S rRNA gene. Next,
816 251-bp paired-end sequencing of the amplicons was performed on a MiSeq system (Illumina)
817 using the MiSeq Reagent v2 500 cycle kit. The paired end sequences obtained were merged,
818 filtered, and denoised using DADA2. Taxonomic assignment was performed using a QIIME2
819 feature-classifier plugin with the Greengenes 13_8 database. The QIIME2 pipeline⁷⁵, version
820 2020.2, served as the bioinformatics environment for the processing of all relevant raw
821 sequencing data.

822

823 **In vivo assay of MP2 Kupffer cell induction by Odoribacteraceae**

824 To establish gnotobiotic mice, germ-free mice received 1×10^8 colony forming units (CFUs)
825 of Odoribacteraceae (Odori) or *Bacteroides stercoris* (Stercoris) via oral gavage twice at days
826 0 and 2. Germ-free mice and gnotobiotic mice were then maintained in individual isolators,
827 respectively, at the animal facilities of Oriental Bio Service, Inc. At day 21, the livers and
828 colorectal contents of germ-free and gnotobiotic mice were harvested for the assays. For
829 assessment of MP2 induction by SPF commensals or by combination of Odori/Stercoris and
830 SPF commensals, mice were treated with ampicillin, vancomycin, neomycin, and
831 metronidazole via drinking water for 6 weeks to deplete gut commensals and reduce MP2
832 population, and then Odori, Stercoris, or vehicle was inoculated into the mice. The mice were
833 housed with SPF mice in the same cage. As for the inoculation of Odori and Stercoris, 1×10^8
834 CFUs of each bacterium was inoculated per mouse via oral gavage for the first 5 days
835 consecutively, and thereafter, every other day until day 19. At day 21, the livers and colorectal
836 contents were harvested for the assays.

837

838 **Measurement of faecal isoallo-lithocholic acid concentration**

839 Faecal contents were suspended in 10 times the volume of 2-propanol containing the internal
840 standard (250 ng/mL LCA-*d*₄). The suspension was homogenised using Precellys (Bertin
841 Technologies) and then incubated for 30 min at 37 °C under sonication. The suspension was

842 centrifuged at $13,000 \times g$ for 5 min at 4 °C. Supernatant was collected for LC-MS/MS analysis.
843 1 μ L of the supernatant was used for the analysis. LC-MS/MS analysis was performed under
844 previously reported conditions²⁶ with slight modifications using a Nexera XR system
845 (Shimadzu, Japan) coupled with an LCMS-8050 triple quadrupole mass spectrometer
846 (Shimadzu) with a heated electrospray ionization source. A separation column, InertSustain
847 C18 (150 mm \times 2.1 mm I.D., 3 μ m; GL Sciences), was used at 40 °C. A mixture of 10 mM
848 ammonium acetate (A) and acetonitrile (B) was used as the mobile phase and the separation
849 was carried out by gradient elution at a flow rate of 0.2 mL/min. The gradient condition was as
850 follows: 14%B, 0–0.5 min; 14–22%B, 0.5–5 min; 22–28%B, 5–28 min; 28–54%B, 28–55 min;
851 54–98%B, 55–66 min; 98%B, 66–70 min; and 14%B, 70–75 min. To operate the LC-MS/MS
852 analysis, we used the following MS parameters: interface voltage, -3kV; interface temperature,
853 300 °C; desolvation line temperature, 250 °C; heat block temperature, 400 °C; nebulizing gas,
854 2 L/min; heating gas, 10 L/min; drying gas, 10 L/min. A deuterated internal standard (LCA-
855 *d*₄) was used to quantify isoallo-LCA. The data analysis was performed using LabSolutions,
856 ver. 5.120 (Shimadzu).

857

858 **Preparation of enhanced green fluorescent protein (eGFP)-labelled *E. coli* and *in vivo*** 859 **challenges**

860 We inserted eGFP DNA into multiple cloning sites of the bacterial vector pQE-60. *E. coli*

861 DH5 α cells (#9057, TaKaRa) were transformed using this recombinant vector and then plated
862 on lysogeny broth medium (#20069-65, Nacalai) containing 100 μ g/mL ampicillin (#19769-
863 64, Nacalai). Single eGFP-positive colonies were picked and further cultured in lysogeny broth
864 medium (#20068-75, Nacalai) containing 100 μ g/mL ampicillin with agitation at 37°C for
865 propagation. The cell density of *E. coli* was measured using BioPhotometer Plus (Eppendorf,
866 Germany) and adjusted to an OD600 of 0.38–0.40. The *E. coli* culture medium (1 mL) was
867 collected and centrifuged at 10,000 \times g for 5 min. The supernatant was discarded, and the pellet
868 was suspended in sufficient PBS to remove any released bacterial components. Subsequently,
869 the *E. coli* suspension was re-centrifuged at 10,000 \times g for 5 min. The supernatant was
870 discarded, and the pellet was resuspended in 500 μ L PBS. Then, 100 μ L of the suspension was
871 slowly injected into the mice via the PV using an ultra-fine 29 G insulin syringe (#SS-
872 10M2913A, TERUMO). Thereafter, the liver was immediately harvested and fixed in 4% PFA
873 before immunofluorescence staining.

874

875 **In vitro assay of bacterial capture by liver-resident macrophages**

876 The eGFP-labelled *E. coli* density was measured using BioPhotometer Plus and adjusted to
877 an OD600 of 0.19 – 0.21. The *E. coli* culture medium (1 mL) was collected, and 400 μ L of an
878 *E. coli*-containing PBS suspension was prepared as described above. Intrahepatic immune cells
879 were collected from the liver (see above), and Kupffer cells were plated onto a 6-well glass-

880 bottom dish (#5816-006, Iwaki) in 3 mL Dulbecco's Modified Eagle Medium (#08459-64,
881 Nacalai) containing 2% FBS and 10 ng/mL macrophage colony-stimulating factor (#315-02,
882 Peprotech) at 37°C for 2 h to allow the Kupffer cells to adhere to the bottom. The cells were
883 then washed to remove any non-adhering cells. The *E. coli* (150 µL) suspension was added to
884 the Kupffer cells and incubated for 1 h at 37°C to allow the Kupffer cells to capture the *E. coli*.
885 Subsequently, the cells were washed and incubated in cell dissociation Hank's solution (#S-
886 004-B, Millipore) for 10 min at 37°C for collection. The cells were then stained with CD45-
887 PE/Cy7, CD64-PerCP/Cy5.5, F4/80-APC, and MARCO-DyLight405 (see **Supplementary**
888 **Table 1**) and analysed using BD FACS Celesta and FlowJo software.

889

890 **Experimental colitis model**

891 The mice received 1% dextran sodium sulphate (DSS, #160110, MP Biomedicals) via
892 drinking water for 7 days, followed by untreated normal water for 4 days to induce acute
893 colitis⁷⁶. The mice were used for the assays 11 days after starting DSS treatment. Mouse body
894 weights were measured on days 0, 7, and 11. To generate the chronic colitis model, the mice
895 received three cycles of 1% DSS via drinking water for 7 days, followed by untreated normal
896 water for 7 days⁷⁷. After the third DSS treatment, normal water was given for 4 days. The livers
897 were harvested for the assays 39 days after the start of the first DSS treatment. Mouse body
898 weights were measured on days 0, 7, 14, 21, 28, 35, and 39.

899

900 **Diet-induced NAFLD/NASH model**

901 Mice were fed ad libitum for up to 8 weeks with a 0.1 % methionine and choline-deficient
902 high-fat (60 kcal%) diet^{78,79} (Research Diets, A06071302) to induce the non-alcoholic fatty
903 liver disease and steatohepatitis (NAFLD/NASH). Peripheral blood and livers were harvested
904 every 2 weeks for the assays. Serum samples were prepared for the biochemical analyses. Liver
905 samples were fixed in 4 % paraformaldehyde for 2 days. Some parts were embedded in paraffin,
906 and the others were dehydrated with 15% and 30% sucrose solutions and embedded in O.C.T.
907 Compound. Paraffin-embedded livers were used for Masson trichrome staining and O.C.T.
908 Compound-embedded frozen livers were used for immunofluorescence staining.

909

910 **Human samples and immunofluorescence staining**

911 The Institutional Review Board for Clinical Research at Osaka University Hospital approved
912 this study. Informed consent for surgical intervention was obtained from each patient. Control
913 or PSC liver tissues, located far from any colorectal cancer metastatic lesion, were obtained
914 from patients who underwent surgical resection at Osaka University Hospital. These tissue
915 specimens were immediately fixed in 10% formalin and then processed routinely for paraffin
916 embedding. Paraffin-embedded sections were cut at a thickness of 4 µm, deparaffinised in
917 cresol and ethanol, and rinsed in PBS. Antigens were retrieved by heating with EnVision FLEX

918 Target Retrieval Solution, High pH (Dako, Agilent) at 110 °C for 15 min. After washing in
919 deionised distilled water and EnVision FLEX Wash Buffer (Dako, Agilent), the sections were
920 incubated in Antibody Diluent/Block (Akoya Biosciences) for 30 min at RT. Primary antibodies
921 were diluted in the Antibody Diluent/Block. After incubation with antibodies at 4 °C overnight,
922 the sections were washed in Wash Buffer, incubated with Opal Polymer HRP Ms + Rb (Akoya
923 Biosciences) for 30 min at RT, and washed in Wash Buffer. Next, the sections were incubated
924 with Opal fluorophores (Akoya Biosciences) for 10 min, then washed in Wash Buffer and
925 rinsed in PBS. For the subsequent antibody applications, the slides were heated again to remove
926 the antibody complexes after incubation, followed by the steps described above. Finally, after
927 heating, the slides were washed with Wash Buffer and then cover-slipped in Fluoro-KEEPER
928 Antifade Reagent, Non-Hardening Type with DAPI (Nacalai Tesque). The primary antibodies
929 used included anti-MARCO (Sigma-Aldrich) (1:500 dilution), anti-CD68 (Dako, Agilent)
930 (1:100 dilution), and anti-CK19 (Cell Marque) (1:100 dilution). The fluorophores used
931 included Opal 690, Opal 570, and Opal 520 at 1:100 dilution in 1 × Plus Amplification Diluent
932 (Akoya Biosciences). Imaging was performed using a confocal microscope (A1R, Nikon) with
933 a ×20 objective lens (CFI Plan Apo VC, numerical aperture: 0.75, Nikon). The antibodies used
934 for human tissue staining are listed in **Supplementary Table 1**.

935

936 **Statistics and Reproducibility**

937 All line graphs are presented as means \pm standard error of the mean (SEM). All box plots
938 present the means, medians, smallest observations, lower and upper quartiles, and largest
939 observations. Basically, nonparametric paired and unpaired two-sided Mann–Whitney U tests
940 were applied for comparisons between the two groups. Statistical analyses were performed
941 using R (version 4.1.2). Experiments were repeatedly performed to ensure the reproducibility
942 of our observations. All results were determined from at least two independent experiments
943 (twice: Figs. 1e-h, 2a, 4a-d, f, Extended Data Figs. 5a-h, 6a-h, 7a-c, 10a-c, 11b-d, g-j,
944 Supplementary Figs. 1a-c, 2a-c, 3d, 8a-d, and three or more times: Figs. 1a-d, i, 2b-d, 3a-f, 4e,
945 g, h, 5b-i, Extended Data Figs. 1a, b, 2c-e, 4a-c, 7e, f, 8b-e, 9b-p, 11f, Supplementary Figs. 2d,
946 e, 3c, 4a-d, 5a-c).

947

948 **Data availability**

949 Visium and single-cell RNA sequencing data have been deposited in the NCBI Gene
950 Expression Omnibus (GEO) database under the accession numbers GSE213388 and
951 GSE213165 [<https://www.ncbi.nlm.nih.gov/geo/query/acc.cgi>], respectively. For the
952 reanalysis of mouse liver single-cell RNA sequencing and Visium, we obtained the datasets
953 from the GEO (the accession number: GSE192742 and URL:
954 <https://www.ncbi.nlm.nih.gov/geo/query/acc.cgi>)⁹. For the reanalysis of human single-cell
955 RNA sequencing, we obtained the data of human liver CD45⁺ cells from eight patients (four

956 normal and four cirrhotic livers) from the GEO (the accession numbers: GSM4041150,
957 GSM4041153, GSM4041155, GSM4041160, GSM4041161, GSM4041166, GSM4041168,
958 GSM4041169 and URL: <https://www.ncbi.nlm.nih.gov/geo/query/acc.cgi?acc=GSE136103>)¹⁵.
959 For the reanalysis of mouse liver and intestine single-cell RNA sequencing, we obtained the
960 datasets from Mouse Cell Atlas⁸⁰ [<https://bis.zju.edu.cn/MCA/>]. All other data in this study are
961 available from the corresponding author upon reasonable request.

962

963 **Code availability**

964 All source codes for the Visium and single-cell analyses are available from the GitHub
965 repository [<https://github.com/OU-ICB/YMiyamoto2023>].

966 **Methods references**

- 967 51. Adachi, O. *et al.* Targeted disruption of the MyD88 gene results in loss of IL-1- and IL-
968 18-mediated function. *Immunity* **9**, 143–150 (1998).
- 969 52. Victora, G. D. *et al.* Germinal center dynamics revealed by multiphoton microscopy
970 with a photoactivatable fluorescent reporter. *Cell* **143**, 592–605 (2010).
- 971 53. Madisen, L. *et al.* A robust and high-throughput Cre reporting and characterization
972 system for the whole mouse brain. *Nat. Neurosci.* **13**, 133–140 (2010).
- 973 54. Arredouani, M. *et al.* The scavenger receptor MARCO is required for lung defense
974 against pneumococcal pneumonia and inhaled particles. *J. Exp. Med.* **200**, 267–272
975 (2004).
- 976 55. Atarashi, K. *et al.* Induction of colonic regulatory T cells by indigenous Clostridium
977 species. *Science* **331**, 337–341 (2011).
- 978 56. Faust, N., Varas, F., Kelly, L. M., Heck, S. & Graf, T. Insertion of enhanced green
979 fluorescent protein into the lysozyme gene creates mice with green fluorescent
980 granulocytes and macrophages. *Blood* **96**, 719–726 (2000).
- 981 57. Jung, S. *et al.* Analysis of fractalkine receptor CX₃CR1 function by targeted deletion
982 and green fluorescent protein reporter gene insertion. *Mol. Cell. Biol.* **20**, 4106–4114
983 (2000).
- 984 58. Kamran, P. *et al.* Parabiosis in mice: a detailed protocol. *J. Vis. Exp.* 1–5 (2013).

- 985 59. Tavares, A. J. *et al.* Effect of removing Kupffer cells on nanoparticle tumor delivery.
986 *Proc. Natl. Acad. Sci. U. S. A.* **114**, E10871–E10880 (2017).
- 987 60. Xu, M. *et al.* c-MAF-dependent regulatory T cells mediate immunological tolerance to
988 a gut pathobiont. *Nature* **554**, 373–377 (2018).
- 989 61. Ogawa, Y. *et al.* Gut microbiota depletion by chronic antibiotic treatment alters the
990 sleep/wake architecture and sleep EEG power spectra in mice. *Sci. Rep.* **10**, 19554
991 (2020).
- 992 62. Hie, B., Bryson, B. & Berger, B. Efficient integration of heterogeneous single-cell
993 transcriptomes using Scanorama. *Nat. Biotechnol.* **37**, 685–691 (2019).
- 994 63. Wolf, F. A., Angerer, P. & Theis, F. J. SCANPY: large-scale single-cell gene expression
995 data analysis. *Genome Biol.* **19**, 15 (2018).
- 996 64. Huang, D. W., Sherman, B. T. & Lempicki, R. A. Systematic and integrative analysis
997 of large gene lists using DAVID bioinformatics resources. *Nat. Protoc.* **4**, 44–57 (2009).
- 998 65. Schneider, C. A., Rasband, W. S. & Eliceiri, K. W. NIH Image to ImageJ: 25 years of
999 image analysis. *Nat. Methods* **9**, 671–675 (2012).
- 1000 66. Lämmermann, T. *et al.* Neutrophil swarms require LTB4 and integrins at sites of cell
1001 death in vivo. *Nature* **498**, 371–375 (2013).
- 1002 67. Uderhardt, S., Martins, A. J., Tsang, J. S., Lämmermann, T. & Germain, R. N. Resident
1003 macrophages cloak tissue microlesions to prevent neutrophil-driven inflammatory

- 1004 damage. *Cell* **177**, 541-555 (2019).
- 1005 68. Medaglia, C. *et al.* Spatial reconstruction of immune niches by combining
1006 photoactivatable reporters and scRNA-seq. *Science* **358**, 1622–1626 (2017).
- 1007 69. Bonnardel, J. *et al.* Stellate cells, hepatocytes, and endothelial cells imprint the Kupffer
1008 cell identity on monocytes colonizing the liver macrophage niche. *Immunity* **51**, 638-
1009 654 (2019).
- 1010 70. Hao, Y. *et al.* Integrated analysis of multimodal single-cell data. *Cell* **184**, 3573-3587
1011 (2021).
- 1012 71. Xiong, X. *et al.* Landscape of intercellular crosstalk in healthy and NASH liver revealed
1013 by single-cell secretome gene analysis. *Mol. Cell* **75**, 644-660 (2019).
- 1014 72. Aizarani, N. *et al.* A human liver cell atlas reveals heterogeneity and epithelial
1015 progenitors. *Nature* **572**, 199–204 (2019).
- 1016 73. Liew, P. X., Lee, W.-Y. & Kubes, P. iNKT cells orchestrate a switch from inflammation
1017 to resolution of sterile liver injury. *Immunity* **47**, 752-765 (2017).
- 1018 74. Ju, W. *et al.* Reference gene selection and validation for mRNA expression analysis by
1019 RT-qPCR in murine M1- and M2-polarized macrophage. *Mol. Biol. Rep.* **47**, 2735–2748
1020 (2020).
- 1021 75. Bolyen, E. *et al.* Reproducible, interactive, scalable and extensible microbiome data
1022 science using QIIME 2. *Nat. Biotechnol.* **37**, 852–857 (2019).

- 1023 76. Mathies, F. *et al.* Colitis promotes a pathological condition of the liver in the absence of
1024 Foxp3⁺ regulatory T cells. *J. Immunol.* **201**, 3558–3568 (2018).
- 1025 77. Kwon, J., Lee, C., Heo, S., Kim, B. & Hyun, C.-K. DSS-induced colitis is associated
1026 with adipose tissue dysfunction and disrupted hepatic lipid metabolism leading to
1027 hepatosteatosis and dyslipidemia in mice. *Sci. Rep.* **11**, 5283 (2021).
- 1028 78. Matsumoto, M. *et al.* An improved mouse model that rapidly develops fibrosis in non-
1029 alcoholic steatohepatitis. *Int. J. Exp. Pathol.* **94**, 93–103 (2013).
- 1030 79. Ikawa-Yoshida, A. *et al.* Hepatocellular carcinoma in a mouse model fed a choline-
1031 deficient, L-amino acid-defined, high-fat diet. *Int. J. Exp. Pathol.* **98**, 221–233 (2017).
- 1032 80. Fei, L. *et al.* Systematic identification of cell-fate regulatory programs using a single-
1033 cell atlas of mouse development. *Nat. Genet.* **54**, 1051–1061 (2022).
- 1034

1035 **Acknowledgments**

1036 We appreciate Dr. Ronald N. Germain (NIAID/NIH, Maryland, USA) for critically reviewing
1037 the manuscript. We thank Drs. Y. Yahara, S. Kameoka, F. Sugihara, T. Sudo, T. Ariyoshi, Bo
1038 Li, and Ms. M. Shirazaki, Ms. F. Okiji, Ms. A. Sakai for their instructive comments and
1039 technical assistances. This work was supported by CREST (JPMJCR15G1 to M.I.) from Japan
1040 Science and Technology (JST) Agency; Grant-in-Aid for Scientific Research (S) (19H05657
1041 to M.I.), for Transformative Research Areas (A) (20H05901 to M.I.), for International Leading
1042 Research (22K21354 to M.I.), for JSPS Fellows (21J13888 to Y.M.) and Research Activity
1043 Start-up (22K20760 to Y.M.) from the Japan Society for the Promotion of Science (JSPS); the
1044 Innovative Drug Discovery and Development Project (JP21am0401009 to M.I.) and the
1045 Program on the Innovative Development and the Application of New Drugs for Hepatitis B
1046 (JP23fk0310512 to M.I.) from Japan Agency for Medical Research and Development
1047 (AMED); and Uehara Memorial Foundation (to M.I.). Cartoons in this manuscript were created
1048 using Biorender.com. We would like to thank Editage (www.editage.jp) for English language
1049 editing.

1050

1051 **Author contributions**

1052 Y.M. conceived the original idea of this study. Y.M. and M.I. devised the concrete concept.
1053 Y.M., J.Kikuta, and M.I. designed the experiments. Y.M. conducted all of the experiments and

1054 data analyses with assistance from J.Kikuta, T.M., T.H., K.F., Y.U. and E.Y. D.M. and D.O.
1055 processed the sequence data. Y.C.L., S.S. and D.O. established a new data processing method
1056 for spatial transcriptomics. S.K. and H.E. collected and provided the human liver samples and
1057 T.M. and E.M. performed the immunofluorescence staining. K. Tryggvason generated *Marco*⁻
1058 ⁻ mice. T.S. maintained them and assisted with experiments using *Marco* knockout mice. K.A.
1059 and K.H. isolated and provided *Odoribacteraceae* Strain#21. T.Y. and J.Kunisawa measured
1060 concentrations of isoallo-lithocholic acid in faeces. H.K. and K. Takeda supervised the
1061 experiments and analyses pertaining to gut commensal microbes. Y.M. wrote the initial draft,
1062 and Y.M., J.Kikuta and M.I. revised the final draft.

1063

1064 **Competing interests**

1065 The authors declare no competing financial interests.

1066

1067 **Additional information**

1068 Supplementary Information is available for this paper.

1069 Correspondence and requests for materials should be addressed to Masaru Ishii

1070 (mishii@icb.med.osakau.ac.jp)

1071 **Extended Data Figure Legends**

1072

1073 **Extended Data Fig. 1. Spatial heterogeneity in neutrophil adhesion in the steady-state**

1074 **liver. a**, Representative intravital image [left, green: neutrophils, red: Qtracker655 (blood

1075 vessels), and blue: SHG (tissue collagens)] and neutrophil tracks (right, individual colours

1076 mean individual cell tracks). Tracks of neutrophils that adhered to the tissue for over 10 min

1077 are shown. Scale bar: 100 μm . **b**, Numbers of the neutrophil tracks within each zones ($n = 7$).

1078 The quantitative data are presented as means (asterisk) with medians, smallest observations,

1079 lower and upper quartiles, and largest observations. Statistical significance was determined

1080 using unpaired two-sided Mann–Whitney U test.

1081

1082 **Extended Data Fig. 2. Spatial heterogeneity in monocyte/macrophage responses to the**

1083 **laser-induced tissue damage in the liver. a,** Timeline of neutrophil and monocyte responses

1084 post the laser-induced tissue damage. **b,** Experimental design to quantify

1085 monocyte/macrophage accumulations at the laser-induced damaged sites. **c,d,** Representative

1086 intravital images of in situ inflammatory responses by monocytes/macrophages upon the laser-

1087 induced damages under control (c, n = 13) and clodronate liposome-treated (resident

1088 macrophage-depleted) conditions (d, n = 10) [green: monocytes/macrophages, white: damaged

1089 sites (autofluorescence), and blue: SHG (tissue collagens)]. Scale bar: 100 μm . Quantified

1090 accumulation scores of monocyte/macrophage at the lesions are shown (right). **e,** PV/CV ratio

1091 of monocyte/macrophage accumulation at 24 h post-laser ablation under control (n = 13) and

1092 resident macrophage-depleted (n = 10) conditions, indicating spatial polarisation of

1093 accumulation: > 1 and < 1 indicate bias towards PV and CV zones, respectively. All quantitative

1094 data are presented as means (asterisk) with medians, smallest observations, lower and upper

1095 quartiles, and largest observations. Statistical significance was determined using paired (c, d)

1096 and unpaired (e) two-sided Mann–Whitney U tests.

1097

1098 **Extended Data Fig. 3. Reanalysis to identify the Marco⁺ Kupffer cell subset (MP2) using**

1099 **public mouse and human databases. a,** Reproduction of Uniform Manifold Approximation

1100 and Projection (UMAP) depicting distinct myeloid cell clusters **identified** in the mouse liver

1101 cell atlas. The Kupffer cell cluster was further analysed for isolating subclusters. **b,** Density of

1102 *Marco*- (**left**) and *Il10*- (**right**) expressing cells in each Kupffer cell subcluster. Subclusters 8,

1103 10 and 17 should be the MP2. **c,** Reproduction of UMAP depicting the liver zonation in the

1104 mouse liver cell atlas. **d,** Density of *Marco*⁺ *Clec4f*⁺ spots on the liver zonation plot (left). Violin

1105 plot showing quantification of the densities in each zone (right). Statistical significance was

1106 determined using one-sided Student's t-test and resultant *p*-values were corrected using the

1107 Benjamini-Hochberg method. **e,** Summary of **human** sample information (**left**). tSNE plot

1108 depicting distinct immune cell clusters (**right**). All single-cell data from healthy and cirrhotic

1109 samples were integrated and represented on the same tSNE plot. Each cluster was assigned to

1110 the known cell types based on marker genes (**Supplementary Table 3**). The numbers in

1111 brackets indicate the cluster number. Resident macrophages include three clusters. **f,** Gene

1112 expression of *CD68* (left), a human macrophage marker, *MARCO* (centre), and *IL10* (right)

1113 was visualised with an R package 'Nebulosa' (Kernel Gene-Weighted Density Estimation). **g,**

1114 Percentage of MARCO⁺ IL10⁺ cells to total macrophages under healthy and cirrhotic

1115 conditions. Data are presented as means (asterisk) with medians, smallest observations, lower

1116 and upper quartiles, and largest observations. Statistical significance was determined using
1117 unpaired two-sided Mann–Whitney U test.

1118

1119 **Extended Data Fig. 4. Relationship between Marco and IL-10 expressions in Kupffer cells.**

1120 **a**, Transcriptional activity of *Il10* in Marco⁻ (MP1) and Marco⁺ (MP2) Kupffer cells visualised
1121 using *Il10*-Venus mice (n = 7). To confirm the background noise, we used wild-type mice as
1122 the negative control (n = 5). Venus expression was detected using AlexaFluor647-conjugated
1123 anti-Venus antibody to avoid the influence of autofluorescence. Mean fluorescence intensity
1124 (MFI) of AlexaFluor647 (from *Il10*-venus) was measured for statistical comparison. **b**,
1125 Correlation between Marco and *Il10*-venus expressions. ‘R’ indicates the correlation
1126 coefficient. The error bands mean 95% confidence interval. **c**, Relative mRNA expression of
1127 *Il10*, *Il1rn* and *Tgfb1* to *Gapdh* in total Kupffer cell fraction from Marco^{+/+} control (n = 7-9)
1128 and Marco^{-/-} (n = 5-9) mice. All data are presented as means (asterisk) with medians, smallest
1129 observations, lower and upper quartiles, and largest observations. Statistical significance was
1130 determined using unpaired two-sided Mann–Whitney U test.

1131

1132 **Extended Data Fig. 5. Interleukin-10 signalling in PV zones suppressively regulates**

1133 **ICAM1-integrin interactions between endothelial cells and neutrophils. a,** Representative

1134 flow cytometry gating to identify the liver sinusoidal endothelial cell (LSEC) subsets. The

1135 histogram shows the ICAM-1 expression levels on each subset. **b,** Mean fluorescence intensity

1136 (MFI) from ICAM-1 on CD117⁺ and CD117⁻ LSECs (n = 4). **c,** Representative

1137 immunofluorescence images of ICAM-1 in the liver tissue (n = 4, blue: E-cadherin⁺ PV zones,

1138 green: ICAM-1). PV, portal vein; CV, central vein. Scale bar : 100 μ m. **d,** MFI from ICAM-1

1139 on CD117⁺ and CD117⁻ LSECs under anti-IL10R and isotype control antibody-treated

1140 conditions (n = 9 and 7, respectively). **e, Fold changes of *Cxcl1* and *Cxcl2* mRNA expressions**

1141 to *Gapdh* in CD117⁺ LSECs, CD117⁻ LSECs, and Kupffer cells from anti-IL10R and isotype

1142 control antibody-treated mice (n = 7 and 6, respectively). **Data were standardized to ensure a**

1143 **control group mean value of '1'.** **f-h,** Analyses of infiltrating neutrophils in the liver under anti-

1144 IL10R and isotype control antibody-treated conditions (n =4, respectively). Representative

1145 staining of integrin α M (Mac-1 or CD11b) on CD45⁺ Mac-1⁺ Ly-6G⁺ neutrophils (f),

1146 percentage of Mac-1^{high} neutrophils (g), and absolute number of neutrophils (h). All data are

1147 presented as means (asterisk) with medians, smallest observations, lower and upper quartiles,

1148 and largest observations. Statistical significance was determined using unpaired two-sided

1149 Mann-Whitney U test.

1150

1151 **Extended Data Fig. 6. In vitro and in vivo assays of *E. coli*-capturing activity of MP1 and**

1152 **MP2 Kupffer cells. a,** Experimental design for in vitro bacteria-capture assay. **b,**

1153 Representative flow cytometry gating for identifying Marco⁻ (MP1) and Marco⁺ (MP2)

1154 Kupffer cells, and comparison of *E. coli*-derived fluorescence signals. **c,** Mean fluorescence

1155 intensity (MFI) of *E. coli*-derived GFP signals in MP1 and MP2 (n = 7). **d,** Experimental design

1156 for in vivo bacteria-capture assay. **e,** Representative immunofluorescence images (n = 3, 9

1157 visual fields, white: *E. coli*, red: F4/80⁺ macrophages, blue: E-cadherin⁺ PV zones) showing *E.*

1158 *coli* localisation in the liver (left and centre). Scale bar: 100 μm. Percentage of *E. coli* numbers

1159 within each zone to total *E. coli* (right). The exact *p*-value is 4.114×10^{-5} . **f,** Representative

1160 immunofluorescence images (n = 3, 15 visual fields, white: *E. coli*, blue: Marco⁻ MP1, and

1161 red: Marco⁺ MP2) showing the *E. coli*-capturing capability of each subset (left). The raw

1162 images were processed using the Imaris software (centre, yellow: *E. coli*, blue: Marco⁻ MP1,

1163 and red: Marco⁺ MP2). Scale bar: 100 μm. Percentage of *E. coli*-capturing Marco⁻ MP1 and

1164 Marco⁺ MP2 to total *E. coli*-capturing cells (right). **g,** Percentage of cells engulfing more than

1165 two *E. coli* in each Kupffer cell subset. **h,** Representative images showing *E. coli* localisation

1166 in the Marco^{+/+} (n = 5, 25 visual fields) and Marco^{-/-} (n = 4, 30 visual fields) livers (left,

1167 yellow: *E. coli*, blue: E-cadherin⁺ PV zones). *E. coli* are shown as spherical spots using the

1168 imaris. Scale bar: 100 μm. Percentage of *E. coli* numbers within each zone to total *E. coli*

1169 (right). The exact p -values are 1.376×10^{-6} (PV) and 1.376×10^{-6} (CV). Data are presented as
1170 means (asterisk) with medians, smallest observations, lower and upper quartiles, and largest
1171 observations. Statistical significance was determined using paired (c) and unpaired (e-h) two-
1172 sided Mann–Whitney U test.

1173

1174 **Extended Data Fig. 7. Identification of gut commensal bacteria that induce MP2 Kupffer**

1175 **cells and involvement of gut commensals in MP2 induction by isoallo-lithocholic acids. a,**

1176 Relative abundance (%) of microbes at the family level (n = 6 and 5 for the SPF-A and SPF-B

1177 groups, respectively). The data were obtained by 16S rRNA-sequencing. **b,** Relative abundance

1178 (%) of each bacterium significantly enriched in “SPF-A” colorectal contents (n = 6 and 5 for

1179 the SPF-A and SPF-B groups, respectively). **c,** Correlation between the relative abundance of

1180 bacterium and the percentage of Marco⁺ Kupffer cells (MP2). ‘R’ indicates the correlation

1181 coefficient. **d,** Graphical protocol for isoallo-lithocholic acid (isoalloLCA) and/or antibiotic

1182 treatments. **e,** Percentage of Marco⁺ cells to total Kupffer cells under DMSO (n = 10),

1183 isoalloLCA (n = 10), and antibiotic/isoalloLCA (n = 13) treatments. **f,** Fold changes of *Il10*

1184 mRNA expression in total Kupffer cells under each condition [DMSO (n = 10), isoalloLCA (n

1185 = 10), and antibiotics/isoalloLCA (n = 9)]. Data were standardized to ensure a control group

1186 mean value of ‘1’. All data are presented as means (asterisk) with medians, smallest

1187 observations, lower and upper quartiles, and largest observations. Statistical significance was

1188 determined using unpaired two-sided Mann–Whitney U test.

1189

1190 **Extended Data Fig. 8. Periportal immunosuppressive Kupffer cells protect against gut**

1191 **commensal-driven liver inflammation related to experimental colitis. a,** Experimental

1192 design; *Marco*^{+/+} and *Marco*^{-/-} mice received 1% dextran sodium sulphate (DSS) via drinking
1193 water for 7 days to induce acute colitis, followed by drinking normal water for 4 days for
1194 recovery. On day 11, the livers were harvested for assays. **b**, Relative mRNA expression of
1195 anti-inflammatory cytokines *Il10* and *Il1rn* in Kupffer cells from *Marco*^{+/+} and *Marco*^{-/-} mice
1196 (n = 6 each). **c**, Representative intravital images of infiltrating inflammatory neutrophils in
1197 *Marco*^{+/+} (left) and *Marco*^{-/-} (right) mice (n = 6 each, green: neutrophils, red: vascular
1198 structures visualised by Qtracker655). Scale bar: 100 μ m. **d**, Quantification of neutrophil
1199 numbers in 100 μ m³ tissues (n = 6, 12 visual fields per condition). Data contain two tissue
1200 sections from different lobes per mouse. **e**, Body weight change showing the percentage of
1201 body weight on day 11 to the original body weight (on day 0) (n = 6 each). All quantitative data
1202 are presented as means (asterisk) with medians, smallest observations, lower and upper
1203 quartiles, and largest observations. Statistical significance was determined using unpaired two-
1204 sided Mann–Whitney U test.

1205

1206 **Extended Data Fig. 9. Periportal immunosuppressive Kupffer cells suppress progression**

1207 **of the non-alcoholic fatty liver disease. a**, Analysis schedule. **b**, Representative Marco and

1208 TIM-4 staining in CD45⁺ CX₃CR1⁻ F4/80⁺ CD64⁺-gated macrophages. **c,d,f,h**, Kinetics of the

1209 frequency of Marco⁺ TIM-4⁺ MP2 Kupffer cells (c), serum AST (d), serum ALT (f), and

1210 neutrophil abundance (h) [Healthy (n = 6-7), NAFLD/NASH 2W (n = 9-12), 4W (n = 11-12)

1211 and 6W (n = 8)]. **e,g,i**, Correlation between MP2 frequency and AST (e), ALT (g), and

1212 neutrophil abundance (i) in NAFLD/NASH 2W. 'R' indicates the correlation coefficient. The

1213 error bands mean 95% confidence interval. **j**, Serum AST and ALT levels in NAFLD/NASH-

1214 induced Marco^{+/+} (n = 12, 12, 8 for 2W, 4W, 6W, respectively) and Marco^{-/-} mice (n = 8, 10,

1215 8 for 2W, 4W, 6W, respectively). **k**, Representative Masson trichrome staining of healthy

1216 Marco^{+/+}, NAFLD/NASH-induced Marco^{+/+} and Marco^{-/-} livers. Scale bar: 200 μm. **l**,

1217 Percentage of area occupied by fat droplets around portal veins in NAFLD/NASH 6W:

1218 Marco^{+/+} (n = 5, 8 visual fields) and Marco^{-/-} (n = 5, 10 visual fields). **m**, AST/ALT ratio in

1219 NAFLD/NASH 6W: Marco^{+/+} and Marco^{-/-} mice (n = 8 each). **n**, Representative

1220 immunofluorescence images showing MARCO (green), CD68 (red), and CK19 (cyan) in

1221 human livers: NAFLD/NASH (n = 7, 21 visual fields) and normal controls (n = 9, 27 visual

1222 fields). Scale bar: 100 μm. **o**, Absolute numbers of CD68-positive cells (macrophages) per

1223 visual field. **p**, Percentage of Marco-positive cells to total macrophages. All curve graphs

1224 represent means \pm standard error of the mean (SEM). All box plots represent means (asterisk)
1225 with medians, smallest observations, lower quartiles, upper quartiles, and largest observations.
1226 Statistical significance was determined using unpaired two-sided Mann–Whitney U test. The
1227 exact *p*-values are 3.969×10^{-5} (h), 7.693×10^{-5} (p, Normal vs NAFLD), 5.114×10^{-10} (p,
1228 Normal vs NASH).

1229

1230 **Extended Data Fig. 10. Marco⁺ Kupffer cells (MP2) belong to the CD206⁻ ESAM⁻ KC1**

1231 **subset. a**, Representative staining of CD206 and ESAM on Marco⁺ and Marco⁻ Kupffer cells

1232 (CD45⁺ CX₃CR1⁻ F4/80⁺ CD64⁺ population). **b**, Percentage of Marco⁺ cells in KC1 and KC2

1233 (n = 4). **c**, Percentage of total Marco⁺ Kupffer cells, Marco⁺ KC1, and Marco⁺ KC2 in all

1234 Kupffer cells (n = 4). **d**, Diagram illustrating the relationship between KC1/KC2 and MP1/MP2

1235 classifications of Kupffer cells. All box plots represent means (asterisk) with medians, smallest

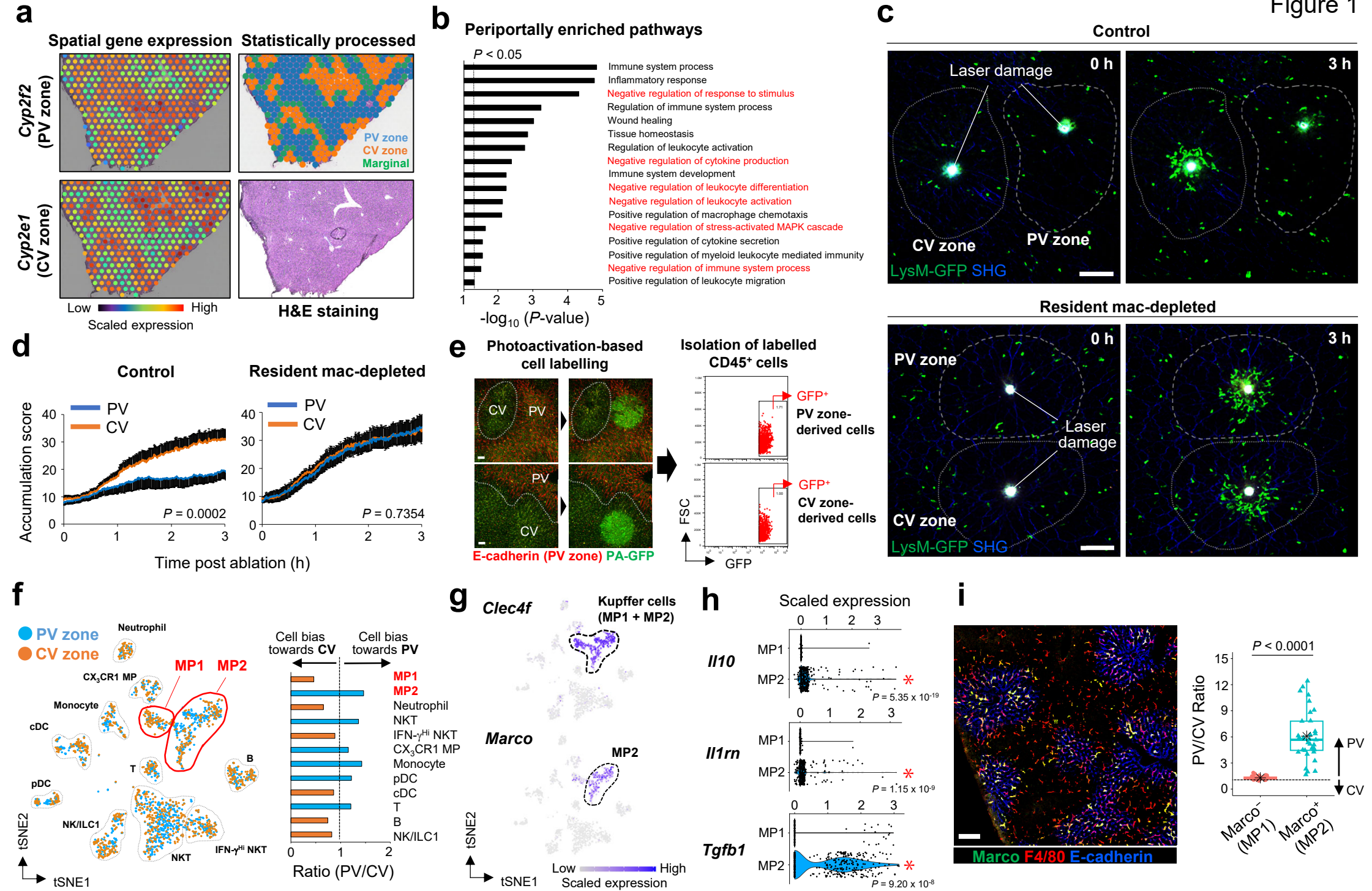
1236 observations, lower quartiles, upper quartiles, and largest observations. Statistical significance

1237 was determined using unpaired two-sided Mann–Whitney U test.

1238

1239 **Extended Data Fig. 11. Marco⁺ immunosuppressive Kupffer cells are supplied by embryo-**
1240 **derived macrophages. a**, Experimental design; generating a parabiosis model to examine the
1241 differentiation from **bone marrow-derived** monocytes into Marco⁺ Kupffer cells (MP2). **b**,
1242 Representative flow cytometry gating of tdTomato⁺ cells on CD45⁺ CX₃CR1⁻ F4/80⁺ CD64⁺
1243 cells in the liver from wild-type parabionts (left). Percentages of Marco⁻ (MP1) and Marco⁺
1244 (MP2) cells to Tomato⁺ Kupffer cells (right, n = 7). **c**, Representative immunofluorescence
1245 images of a wild-type parabiont liver [blue: E-cadherin (PV zones), white: tdTomato (**bone**
1246 **marrow**-derived macrophages), red: F4/80 (Kupffer cells), and green: Marco (MP2)]. Scale
1247 bar: 100 μm (large image) and 20 μm (zoomed images). **d**, Representative immunofluorescence
1248 images of a wild-type parabiont liver [white: tdTomato (**bone marrow**-derived macrophages),
1249 red: CD68 (Kupffer cells), and green: TIM-4 (resident Kupffer cells)]. Scale bar: 100 μm. **e**,
1250 Graphical protocol for analysing resident and **bone marrow-derived (repopulated)** Kupffer cells.
1251 **f**, Representative gating of Kupffer cells in clodronate liposome (CLL)-treated (on day 2) and
1252 untreated mice (left). Absolute number of TIM-4⁺ resident Kupffer cells [right, control (n = 7)
1253 and CLL-treated (n = 6)]. **g**, Representative staining of Marco and TIM-4 on Kupffer cells in
1254 CLL-treated (on week 6) and untreated control mice. **h**, Absolute numbers of TIM-4⁺ resident
1255 Kupffer cells (left) and TIM-4⁻ bone marrow-derived Kupffer cells (right) in CLL-treated (on
1256 week 6, n = 12) and untreated control (n = 7) mice. The exact *p*-value is 3.969×10^{-5} . **i**,

1257 Percentage of Marco⁺ cells in TIM-4⁺ and TIM-4⁻ Kupffer cells in CLL-treated mice (on week
1258 6, n = 12). **j**, Relative mRNA expression of *Il10* to *Gapdh* in TIM-4⁺ and TIM-4⁻ Kupffer cells
1259 from CLL-treated mice (on week 6, n = 8). All data are presented as means (asterisk) with
1260 medians, smallest observations, lower and upper quartiles, and largest observations. Statistical
1261 significance was determined using unpaired (b, f, h) and paired (i, j) two-sided Mann–Whitney
1262 U test.



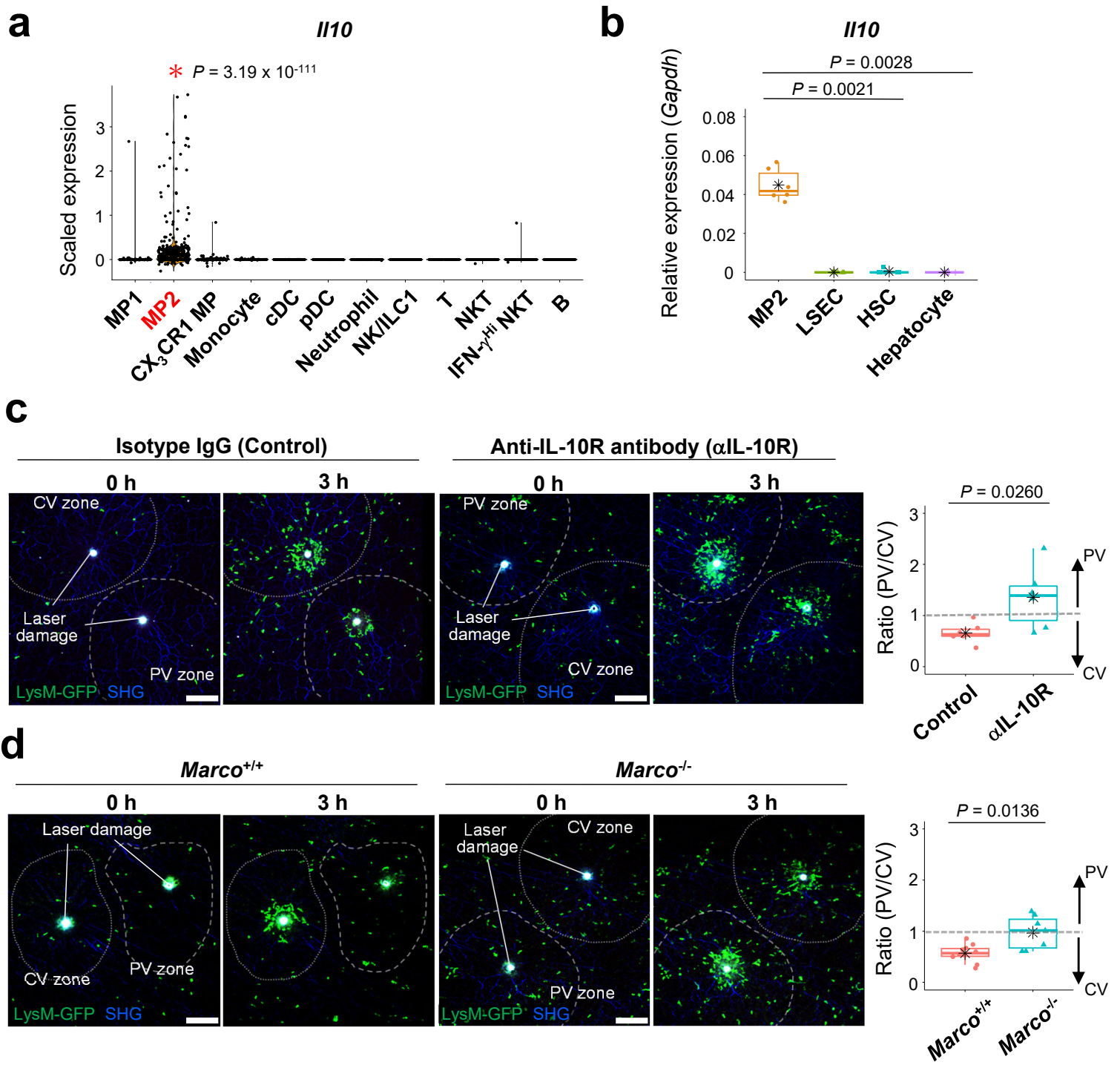


Figure 2

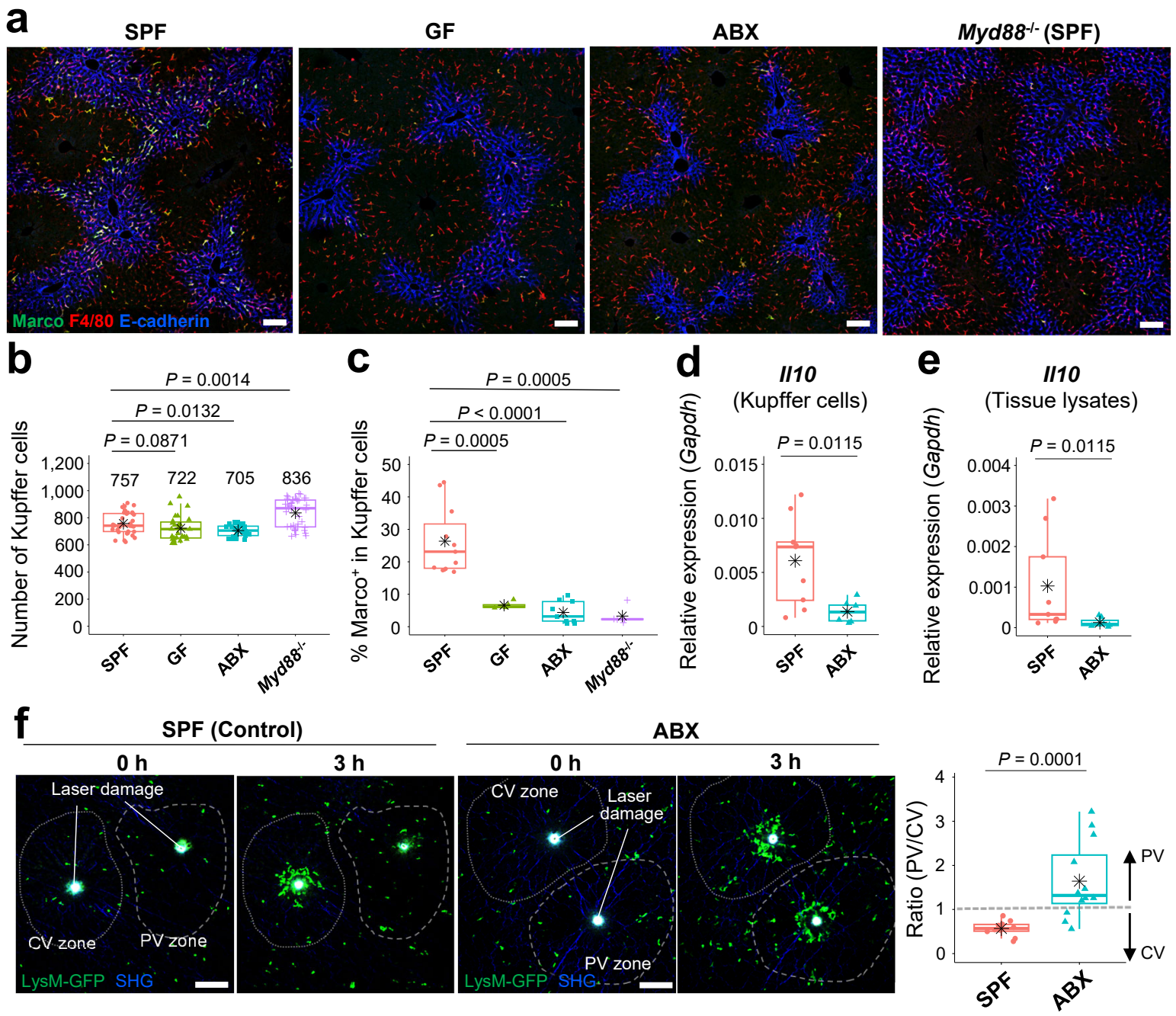


Figure 3

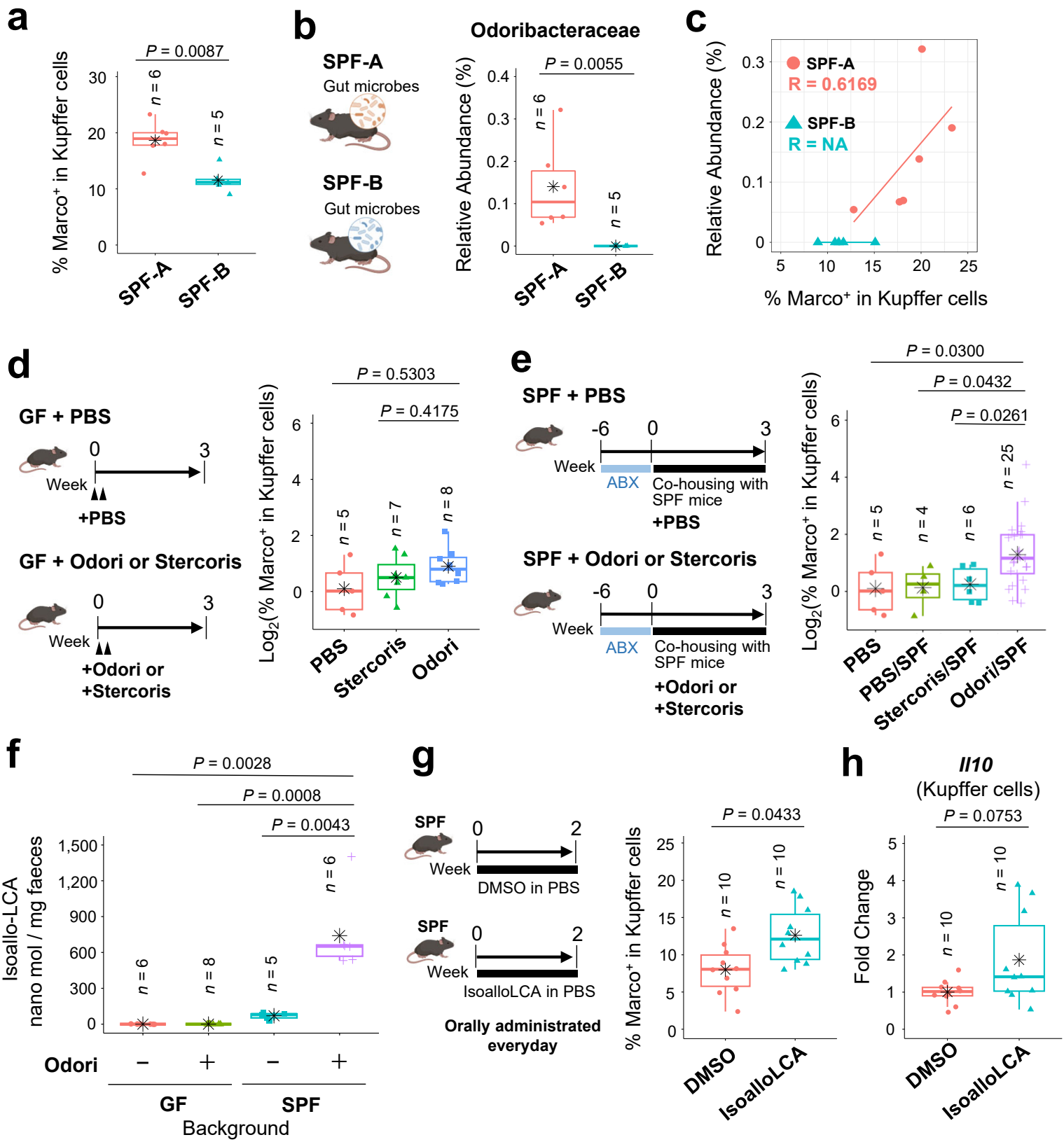


Figure 4

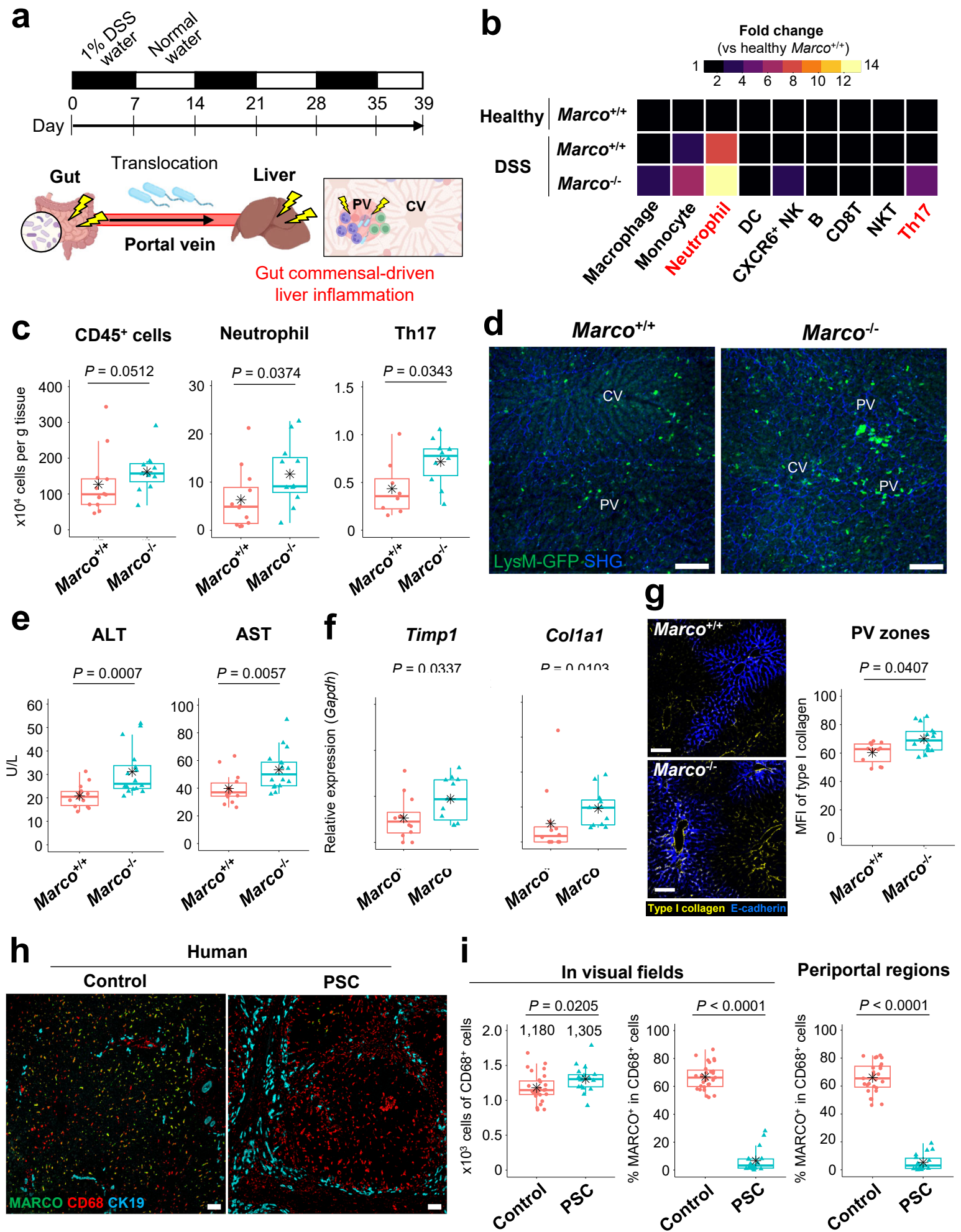


Figure 5